Collisional considerations in axial-collection plasma mass filters

I. E. Ochs,[1,2] R. Gueroult,[3] N. J. Fisch,[1,2] and S. J. Zweben[1,2]

[1)] *Department of Astrophysical Sciences, Princeton University, Princeton, New Jersey 08540*

[2)] *Princeton Plasma Physics Laboratory, Princeton, New Jersey 08543*

[3)] *Laboratoire Plasma et Conversion d'Energie, CNRS, INPT, UPS, 31062 Toulouse, France*

(Dated: 6 March 2017)

The chemical inhomogeneity of nuclear waste makes chemical separations difficult, while the correlation between radioactivity and nuclear mass makes mass-based separation, and in particular plasma-based separation, an attractive alternative. Here, we examine a particular class of plasma mass filters, namely filters in which (a) species of different mass are collected along magnetic field lines at opposite ends of an open-field-line plasma device, and (b) gyro-drift effects are important to the separation process. Using an idealized cylindrical model, we derive a set of dimensionless parameters which provide minimum necessary conditions for effective mass filter function in the presence of ion-ion and ion-neutral collisions. Through simulations of constant-density profile, turbulence-free devices, we find that these parameters accurately describe mass filter performance in more general magnetic geometries. We then use these parameters to inform on the design and upgrade of current experiments, as well as deriving general scalings for the throughput of production mass filters. Importantly, we find that ion temperatures above 3 eV and magnetic fields above 10^4 Gauss are critical to ensure feasible mass filter function when operating at ion densities of 10^{13} cm^{-3}.

I. INTRODUCTION

Nuclear waste remediation and spent nuclear fuel reprocessing involve the separation of unburnt nuclear fuel, highly radioactive waste, and low-activity waste. They are processes made difficult by the extreme heterogeneity of the waste material, since chemical separations are highly species-specific. However, the category of waste, in particular its radioactivity, tends to depend heavily on element mass. Heavier elements (mass number $\mu > 80$ amu), such as Zirconium, Strontium, and Cesium, are far more radioactive than the light elements, such as Oxygen, Aluminum, Sodium, and Iron, which often form the bulk of the waste mass[1]. Furthermore, the longest-lived elements are the transuranics ($\mu > 235$ amu), which can be transmuted into shorter-lived elements once separated[2]. Thus physical separation methods, which differentiate elements based on atomic mass, are potentially attractive.

One such class of physical separation methods is the plasma mass filter (PMF), in which the waste is first ionized, and then separated using a combination of magnetic and electric fields. Such devices have thus far proven extremely useful for separating small quantities of elements differing very slightly in mass. For instance, the calutron[3] was used extensively for separation of U-235 from U-238, both during the Manhattan project and later in the production of fissionable material for power plants. Mass-dependent differences in the ion cyclotron resonance have also been exploited more recently for isotope separation[4].

In contrast to isotope separation, nuclear waste reprocessing requires high-throughput separation of elements with very large mass differences. The crudeness of this separation serves two purposes, both reducing proliferation risk and making higher throughput thermodynamically possible. Unfortunately, the technology for such bulk separation has lagged far behind that necessary for the *creation* of nuclear waste, and an experiment which successfully demonstrates high-throughput separation has yet to be built.

Nevertheless, several PMF concepts have been proposed to tackle the waste reprocessing problem. In most of these proposed PMF designs, the electric field is imposed radially,

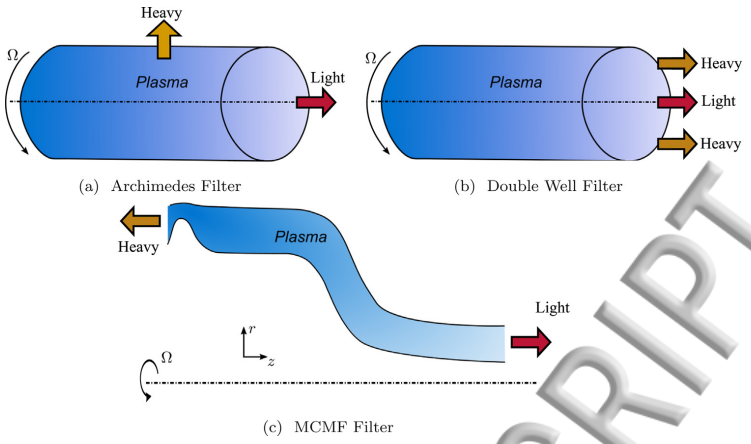

FIG. 1. Schematics of the three plasma mass filter concepts, all of which involve a radial electric field and axial magnetic field. (a) In the band-gap ion mass filter concept[8], heavy ions lie on unconfined radial orbits, and thus exit radially, while light ions remain confined and exit axially. (b) In the double well filter concept[9], heavy ions are confined but localized off-axis, while light ions remain on-axis; thus both species exit axially. However, this concept relies on the ability to finely control the shape of the radial potential profile. (c) In the magnetic centrifugal mass filter (MCMF) concept[10], the coils are configured to provide a mirror throat at large radius. The magnetic field profile is represented by the shape of the plasma in the figure. The mirror throat is shown on the left side of the figure, where the plasma cross-section (following the magnetic field streamlines) becomes narrow, indicating stronger magnetic field (the MCMF magnetic field structure is also illustrated in Fig. 5). Since heavy particles feel the centrifugal force more strongly than the mirror force (and vice-versa for the light particles), heavy particles tend to exit along field lines at large radius, while light particles exit along field lines at low radius. Figure reproduced with permission from J. Hazardous Materials, **297**, 153-159 (2015)[1]. Copyright 2015 Elsevier.

resulting in an $\mathbf{E} \times \mathbf{B}$ rotation around the device axis of symmetry. However, the specifics of the separation vary significantly between designs.

In this paper, we will first review several leading PMF concepts, discussing the strengths and weaknesses of each design in Section II. We will then focus on one particular design, the magnetic centrifugal mass filter (MCMF), which we consider most promising both in terms of near-term experimental feasibility and high-throughput separation potential. Then, in Section III, we will review the design and basic plasma parameters of the Plasma Mass Filter eXperiment (PMFX) at the Princeton Plasma Physics Laboratory. In particular, we will outline the steps necessary to convert the existing device, a standard helicon-generated mirror plasma, to MCMF geometry. This discussion will motivate the core purpose of the paper: to estimate, via simple dimensionless parameters, a set of minimum conditions that must be met to make experimentally-observable mass separation feasible.

Specifically, we examine whether collisional diffusion is likely to force heavy minority ions out of the separating region of the device before separation can take place. Although this condition does not guarantee successful separation, it would be ill-advised to design a device which did not meet this minimal criterium.

Previous simulation-based studies of MCMF feasibility[2,5] have focused on specific parameter sets, at ion temperatures that may be well above the electron temperature range in which PMFs will likely be forced to operate due to line radiation, and particularly at ion temperatures well above the ~ 1 eV ion temperatures typical of laboratory-scale linear devices[6,7] thus the ion-ion collisionality in these studies was far lower than those accessible to potential near-term experiments. In this paper, we extend these studies to a broader parameter regime by developing a set of dimensionless parameters τ which should be greater than one to ensure proper PMF function.

We then compare our analytical results to single-particle simulations, both for a highly-idealized PMF configuration, and for a more realistic PMF configuration. We use a nonlinear

fourth-order Runge-Kutta particle pusher[11], a (modified) Langevin collision model[12] for ion-ion collisions, and a Monte Carlo COM scattering model[13] for neutral collisions. Due to the lack of density profile data for the as-yet-unfinished experimental MCMF, we assume constant density profiles for both ions and neutrals.

We then use these parameters to inform the upgrade design for the Plasma Mass Filter eXperiment (PMFX), identifying minimum necessary conditions for an operating regime in which observable separation can feasibly occur[14]. Although the main focus is on the MCMF, the applicability of each parameter to the alternative PMF concepts is discussed.

Although such an idealized model of collision-induced diffusion cannot capture all effects which might confound mass filter function, and thus not be *sufficient* to guarantee mass filter function, it should provide a set of *necessary* constraints to ensure the possibility of experimental success.

II. REVIEW OF PLASMA MASS FILTER CONCEPTS

The first PMF concept to receive large-scale interest and funding was the DC band-gap plasma mass filter[8], the basis for the Archimedes nuclear waste separator[15]. In this concept, the field configuration results in radially confined orbits for light ions, but unconfined orbits for heavy ions. Thus heavy species can be radially collected and later scraped off, while light species exit axially (Figure 1a).

The radial collection of the heavy species intrinsic to the band-gap filter makes steady-state staging difficult, since the device must have a collection and reionization cycle in order to reprocess the radially collected product. In addition, radial collection necessarily coats large areas of the device with radioactive nuclear material, which can be undesirable.

To address these difficulties, several designs have emerged which aim to collect both species axially, at opposite ends of the device. In the double well mass filter concept[9], a carefully-tailored, quartic radial potential profile

$$\Phi(r) = Cr^4 - Dr^2 \tag{1}$$

is somehow imposed, e.g. by end electrodes. A fluid of ions, however, will respond to the Lorentz-transformed electric potential $\Phi^*(r)$ in their (mass-dependently) $E\times B$-rotating rest frame. For certain choices of the constants C and D, $\Phi^*(r)$ will have an on-axis minimum for light ions, and an off-axis (but still confined) minimum for heavy ions. Thus light ions remain on-axis, while heavy ions congregate in the potential well off-axis (Figure 1b).

Unfortunately, such a detailed radial profiles have thus far proven difficult to reliably control in high-density helicon plasmas[16]. While the overall magnitude of the potential (up to 10s of V/cm) and its rough shape have been varied with some success in low-density helicon plasmas,[17–19] ECR discharges,[20,21] hot cathode discharges,[22] and mirror plasmas,[23,24] the finely-tuned quartically-shaped profiles necessary for double well filter function have yet to be reliably produced.

In the third design, the magnetic centrifugal mass filter[10] (MCMF), magnetic field lines are arranged so that an ion can either exit on-axis in a region of weak magnetic field, or far off-axis in a region of strong magnetic field (Figure 1c). This design requires the field lines to pinch at large radius, which can be seen on the left of the figure, where the plasma narrows (a more detailed look at the MCMF field line geometry will occur later; see Figure 5). The centrifugal force from the rotation of the plasma will thus tend to force heavy ions outward, while light ions will be repelled by the mirror force and tend to exit on-axis. The MCMF is less sensitive to the specifics of the radial potential profile than the double well filter, while also allowing for axial collection of both species (in contrast to the band gap filter). Thus the MCMF is a promising configuration for near-term experiments.

III. THE PLASMA MASS FILTER EXPERIMENT (PMFX)

In its current state, PMFX[14] consists of an RF-generated linear plasma with an on-axis field operating range from 580 to 950 G, and a small secondary chamber that can be fitted with either a high-speed camera or a concentric ring of biasing electrodes. In a typical discharge, the plasma radius is about 5 cm, with a density profile that is peaked on axis at 5 mTorr ($n_n \approx 2 \times 10^{14}$ cm^{-3}) and hollow at 3 mTorr. It is important to note that PMFX does not currently have an MCMF geometry; experimental work up to this point has been focused on establishing the degree of plasma rotation, and controlling this rotation via the end electrodes. This work has shown that the end electrodes can exert some control over the direction and magnitude of the radial electric field; however the range of operating conditions over which this control is possible, as well as the range of achievable electric fields, have yet to be thoroughly established.

The natural next phase of experimentation on PMFX would be to impose the MCMF geometry, which could be accomplished by the construction of a larger secondary chamber, and the addition of a third coil at the far end of the device from the RF antenna. For simplicity, we assume the device (which we denote PMFX* to distinguish it from the current device) would retain its basic plasma parameters, which are notated in Table I and listed in the first column of Table II. This paper will examine the feasibility of such an upgrade, specifically, in whether collisional effects will break the separative effect of the MCMF. Thus, throughout the paper, we will compare this minor modification scenario (PMFX*) with two other engineering scenarios (PMFX-U and PMFX-LD); the parameters for all of which are listed in Table II.

IV. TYPES OF COLLISIONS

Some level of collisionality is necessary for the MCMF to function, since separation requires particles to scatter into the loss cone. However, too much collisionality can break the device in one of two ways.

First, when the collision frequency becomes higher than the gyrofrequency, gyro-drift motion breaks down. Since the MCMF relies on the gyrokinetic response of the plasma to a mirror field, the MCMF will thus cease to adequately function.

Second, even if gyro-drift motion is satisfied, collisions can cause ions to diffuse out of the separation region perpendicular to the magnetic field before they can be extracted along field lines. For recycling species, this would at a minimum reduce the rate and efficiency of ion separation considerably; for a non-recycling species, it would be disastrous.

In this section, we provide approximate expressions for ion-ion and ion-neutral collision rates, since these are the most important types of collisions driving transport in multi-species plasmas. Subsequent sections then use these estimates to derive dimensionless parameters corresponding to the gyro-drift and parallel-exit conditions. Throughout this paper it is assumed that the ion temperature is constant and isotropic throughout the devices modeled. This is a simplifying (and somewhat unrealistic) assumption, since the ion temperature and ion isotropy in helicon plasmas may vary substantially from place to place in the device. However, since we do not yet know what the temperature and isotropy will be in the device, such an idealized model should still be useful in providing a zeroth-order analytical picture of ion behavior.

1. Ion-ion collisions

Mass separation often involves the removal of a heavy minority species from a light majority species. Thus, in contrast to the theory of classical transport in single-ion-species plasmas, ion-ion collisions will be important when considering the motion of the minority species, since the conservation of gyrocenters during a collision will no longer imply a lack

	Description
i	subscript: heavy minority ion
j	subscript: light majority ion
e	subscript: electron
n	subscript: neutral atom
n	density (cm^{-3})
v	velocity (cm/s)
T	temperature (eV)
μ	mass (a.m.u.)
B	magnetic field (Gauss)
L	system length scale (cm)
λ	Coulomb logarithm (~ 8)

TABLE I. Variable and subscript definitions.

	PMFX*	PMFX-U	PMFX-LD
n_j (cm^{-3})	10^{13}	10^{13}	3×10^{11}
n_n (cm^{-3})	10^{14}	10^{14}	10^{13}
B (G)	950	15,000	2500
E (V/cm)	2	5	5
μ_i (a.m.u.)	80	80	80
μ_j (a.m.u.)	40	40	40
T_i (eV)	1	3	1
T_e (eV)	5	5	5
$L_\parallel$ (cm)	40	40	40
$L_\perp$ (cm)	8	12	12

TABLE II. Typical operating parameters for a minor upgrade to the current plasma mass filter experiment[14] (PMFX*) and two potential larger upgrades (PMFX-U and PMFX-LD). PMFX-U is designed to operate at similar densities as PMFX*, whereas PMFX-LD is designed to have similar magnetic fields and ion temperatures at much lower densities. The ratio n_i/n_j of the heavy to light ions is assumed to be small ($< 10\%$). The electric field has been raised in PMFX-U and PMFX-LD to compensate somewhat for the reduction in $E \times B$ velocity from the larger magnetic field, but remains well within the field magnitudes observed in the experimental literature.

of net transport. Since early-phase experiments are likely to use noble gases in place of radioactive waste, we consider the case of Krypton (atomic mass $\mu_i \sim 80$ a.m.u.) in a background plasma of Argon (atomic mass $\mu_j \sim 40$ a.m.u.).

For heavy ions i with velocities in the thermal range, the scattering rate off light background ions j is well-approximated by the low-velocity NRL Formulary formula:

$$\nu_{ii} = \nu_\perp + \nu_\parallel = 2.3 \times 10^{-7} n_j \lambda \mu_j^{1/2} \mu_i^{-1} T_i^{-3/2}. \tag{2}$$

One of the features of Coulomb collisions is the strong inverse scaling ($\nu_{ii} \propto T_i^{-3/2}$) with temperature. Thus in PMFX*, where on average $T_i = 1$ eV, $\nu_{ii} = 1.5 \times 10^6$ s^{-1}, while it is around 5 times smaller in PMFX-U at $T_i = 3$ eV, and around 30 times smaller in PMFX-LD.

2. Ion-neutral collisions

In the low-temperature limit ($T_i \lesssim 3$ eV) typical of helicon plasmas, the ion-neutral collision frequency is approximately independent of velocity. The frequency of a "capture" orbit, in which a random rotation occurs in the ion-neutral COM frame, is given by[25]

$$P_{in} = n_n K_L, \tag{3}$$

where

$$K_L = 8.99 \times 10^{-10} \left(\frac{\alpha_R}{\mu_R}\right)^{1/2} \text{ cm}^3/\text{s}, \tag{4}$$

α_R is the relative polarizability of the atom (11 for Argon), and μ_R is the reduced mass of the two colliding species. This collision frequency results from the well known "polarization cross section."

It is important to note that P_{in} is not directly comparable to ν_{ii}, because the former represents the frequency of COM scattering events, while the latter represents the rate of velocity-space diffusion. To compare them, we should consider the quantity

$$\nu_{in} \equiv P_{in} \min\left(1, \mu_n/\mu_i\right), \tag{5}$$

since this accounts for the number of collisions it will on average take to scatter the ion in velocity space.

The collision frequency ratio is thus given by (taking $\mu_j = \mu_n < \mu_i$)

$$\frac{\nu_{ii}}{\nu_{in}} = 2.6 \times 10^2 \lambda \alpha_R^{-1/2} \left(\frac{\mu_i}{\mu_i + \mu_j}\right)^{1/2} T_i^{-3/2} \left(\frac{n_j}{n_n}\right). \tag{6}$$

Thus, as long as

$$T_i^{3/2} \left(\frac{n_n}{n_j}\right) \ll 260 \lambda \alpha_R^{-1/2}, \tag{7}$$

which will generally be the case for the high-ionization-fraction ($n_j/n_n \geq 10\%$), low temperature ($T_i \leq 3$ eV) plasmas we are interested in, diffusion due to ion-ion collisions will be much greater than that due to ion-neutral collisions. For instance, in PMFX* and PMFX-U, $\nu_{in} = 2.9 \times 10^4$ s^{-1}, and so the collision frequency ratios are 0.019 and 0.10 respectively. In PMFX-LD, we also have $\nu_{in} = 2.9 \times 10^4$, which is on the same order but still less than the ion-ion collision frequency.

Nevertheless, ion-neutral collisions will be of interest to us, because the bulk flow caused by the plasma rotation can (in the limit of low enough plasma-gas momentum coupling) lead to a large relative flow velocity between the ion and neutral populations. This leads to advective (rather than diffusive) transport in the plasma, which will dominate at large perpendicular length scales.

The difference between the advective effect of collisions with neutrals and the diffusive effect of collisions with ions can be seen in the simulations shown in Figure 2. Krypton (80 amu) ions were initialized at $r = 15$ cm, in the presence of a radial E field of 3 V/cm and and axial B field of 10^4 G. They then experienced collisions with an $E \times B$ rotating background of Argon ions (40 amu), with a density of 3×10^{12} cm^{-3} and a temperature of 1 eV (dashed lines). Half of the simulations (solid lines) also included collisions with a stationary background of neutral Argon atoms at $n_n = 3 \times 10^{13}$. The simulation was carried out for both an outwardly-directed (blue) and inwardly-directed (red) electric field. Although the presence of neutrals has little effect on the diffusive motion (i.e. the standard deviation of particle positions), it can have a large effect on the mean particle position, moving the ions to lower electrical potential.

V. GYROCENTER MOTION

Some plasma mass filter designs rely on gyrocenter drift effects, such as the mirror force. If the collision frequency is too high, the gyrocenter motion will be destroyed—in particular, the mirror force disappears in a sufficiently collisional (isotropic-pressure) plasma[26].

For ions to undergo gyrorotation, we must have

$$\frac{2}{3}\nu_{ii} \leq \Omega_i, \tag{8}$$

where ν_{ii} is the scattering rate off background ions, and Ω_i is the cyclotron frequency. Here the factor of 2/3 arises from considering only diffusion perpendicular to the magnetic field.

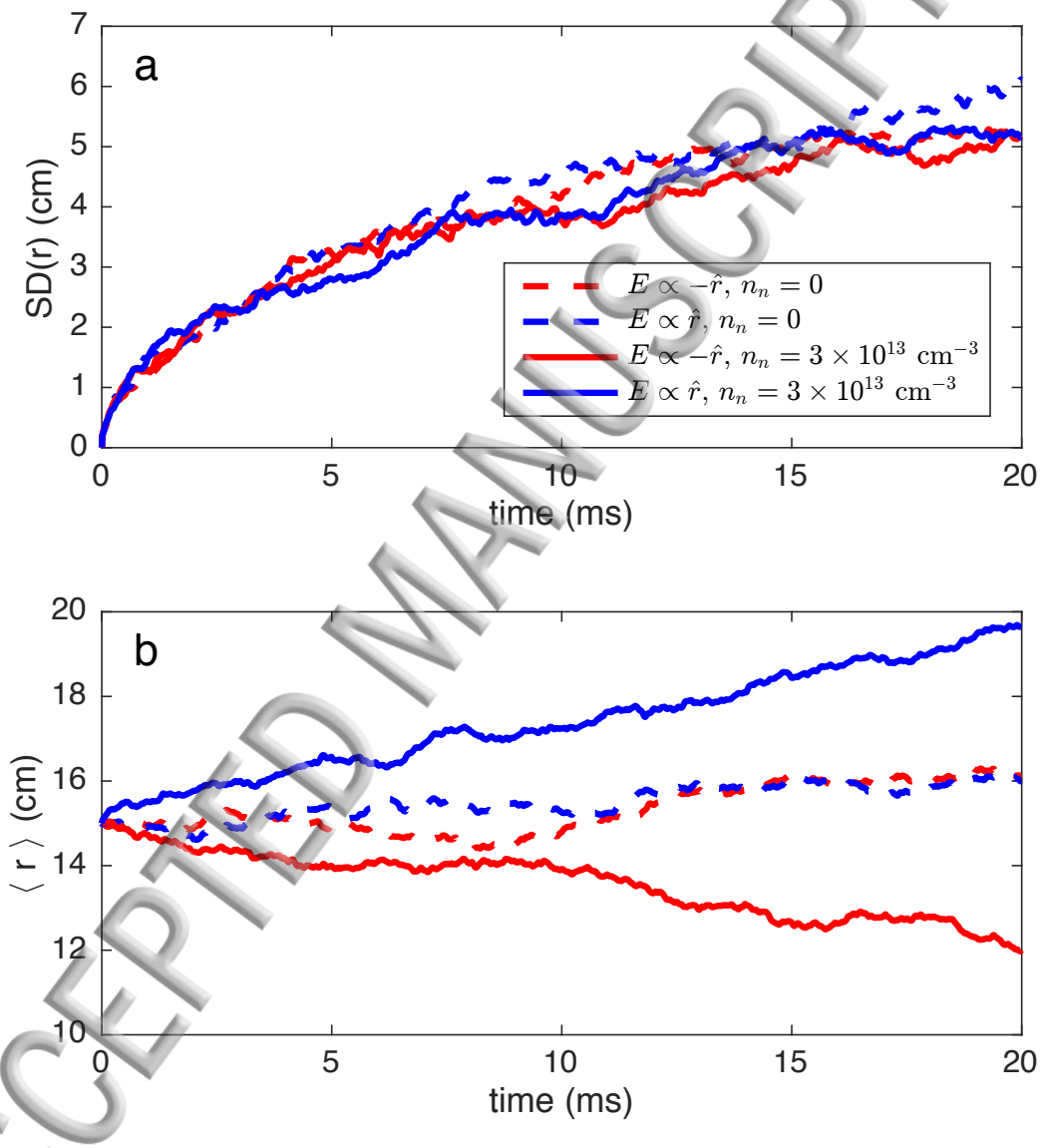

FIG. 2. Evolution (average of 50 simulations per line) of (a) standard deviation and (b) mean of particle radial position as a function of time in a cylindrical, $E \times B$ rotating plasma with a stationary, cold neutral background. Dashed lines indicate $n_n = 0$, solid lines $n_n = 3 \times 10^{13}$ cm^{-3}. Blue lines indicate $E_r = 3$ V/cm, red lines $E_r = -3$ V/cm. Remaining shared parameters are $T_i = 1$ eV, $B = 1 \times 10^4$ G, $\mu_i = 80$, $\mu_j = 40$, $n_e = 3 \times 10^{12}$ cm^{-3}. Diffusion due to neutrals is weak, as can be seen from the minimal impact they make on the standard deviation. Nevertheless, the advective motion caused by ion-neutral collisions results in biased particle motion in the direction of lower electrical potential energy, as can be seen in the graph of average position over time. Thus over a length scale of $L_\perp \lesssim 2$ cm, the ion-ion diffusion will dominate, while on a length scale $L_\perp \gtrsim 8$ cm, ion-neutral advection will dominate.

The gyrofrequency is given by

$$\Omega_i = 9.6 \times 10^3 \mu_i^{-1} B. \tag{9}$$

Thus, the quantity $\tau_M \equiv \Omega_i/\nu_{ii}$ must be greater than one. Combining our formulae for Ω_i and ν_{ii}, we thus have:

$$\tau_M \equiv \frac{3}{2}\frac{\Omega_i}{\nu_{ii}} = 6.2 \times 10^{10} B T_i^{3/2} \lambda^{-1} \mu_j^{-1/2} n_j^{-1}. \tag{10}$$

For the PMFX*, we have $\tau_M = 0.12$, so we should not expect to see gyro-center drift motion. Thus only filtering processes which work when assuming a fluid plasma model will likely be observed on the current device. On PMFX-U and PMFX-LD, in contrast, we have $\tau_M = 12$ and $\tau_M = 10$ respectively, meaning that ions undergo around 10 gyro-rotations before scattering significantly in velocity space.

VI. PARALLEL TRANSPORT TIMESCALES

Once we know that our plasma is undergoing gyrocenter drift motion, it is necessary to ensure that the large majority of particles exit the plasma along field lines, before they are forced out radially by collisional effects. Thus it is necessary to compare the timescales of parallel vs perpendicular transport, the first of which we consider in this section.

For the following two sections, we consider the extremely idealized model in Figure 3. Thus we model the separation region as a cylindrical annulus of thickness $L_\perp$ and length $L_\parallel$, with a constant magnetic field oriented along $\hat{z}$ and a constant electric field along $\hat{r}$. Such fields are consistent with those produced by concentric end electrodes in the limit of large conductivity parallel and negligible conductivity perpendicular to the magnetic field. The magnetic field for the idealized model in Secs. VI and VII is assumed to pinch in an extremely narrow region at the ends, so that there is a localized mirror force confining ions however, this only becomes important when the collisionality is sufficiently low, which is not

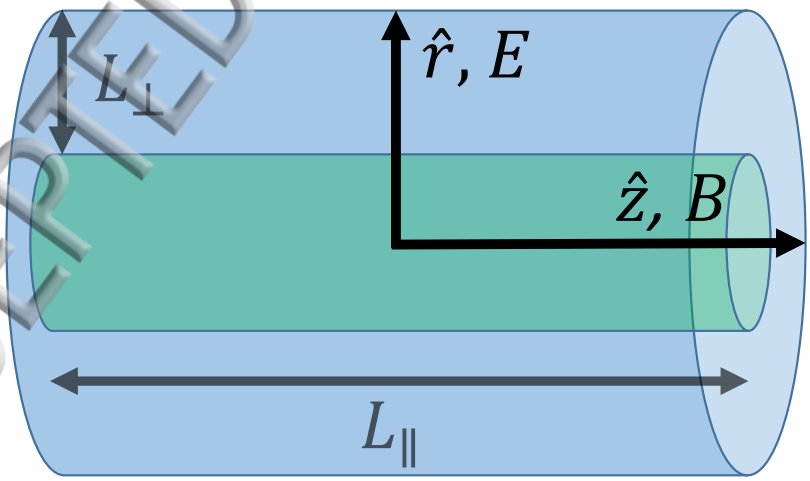

FIG. 3. Relevant length scales and fields in idealized PMF model. Ions must remain confined in an annular region of width $L_\perp$ within the blue cylinder and outside the green one while they exit axially. The magnetic field is uniform, except in a narrow region on either end of the device where it pinches sharply, resulting in mirror confinement. In this paper, we focus on the transport of the minority heavy ions, which are more likely to be long-lived, radioactive isotopes. The constant E field points radially, perpendicular to the axial constant B field.

treated explicitly in these sections. These mirror fields are used to model the existence of a more general loss cone, which arises from both the mirror force and the centrifugal force. The full MCMF magnetic geometry including mirror effects and collisionality is simulated in Sec. IX.

Collisional parallel transport of heavy minority ions in such a device separates naturally into two main regimes. The first regime corresponds to low collisionality, where the collision time ν_{ii}^{-1} is much longer than the bounce time $t_{\text{bounce}} = L_\parallel / v_{thi}$. In this case, just as in fusion mirror transport,[27] the typical confinement time will be the time to scatter into the loss cone.

The second regime occurs when the bounce time is much longer than the collision time. In this case, transport is largely diffusive, with the ion experiencing a random walk due to collisions.

A. Multi-bounce parallel transport

In the regime of extremely low collisionality, where

$$\nu_{ii} t_{\text{bounce}} \ll 1, \tag{11}$$

the characteristic multi-bounce exit time is the time to scatter into the loss cone,[27] i.e.

$$t_{\parallel MB} = \nu_{ii}^{-1} = 4.3 \times 10^6 n_j^{-1} \lambda^{-1} \mu_j^{-1/2} \mu_i T_i^{3/2}. \tag{12}$$

This is the regime originally envisioned for the MCMF. If this were the parallel exit mechanism for PMFX*, PMFX-U, or PMFX-LD, the parallel confinement times would be on the order of 0.67, 3.6, and 23 microseconds respectively. However, because the mean free path v_{thi}/ν_{ii} in each of these devices is much shorter than the parallel device scale $L_\parallel$, the particle will collide long before it completes a transit of the device, invalidating the loss-cone-scattering model.

B. Diffusive parallel transport

The fact that all of the proposed parameter sets operate far from the multi-bounce regime is no coincidence. Because of the low temperatures at which mass filters must operate, and the densities required to reliably produce a plasma, the plasma is likely to be highly collisional, making it difficult to access the multi-bounce regime in Eq. (11). Instead, the minority species will diffuse out axially, with a diffusion coefficient given by

$$D_\parallel = \frac{3 v_{thi}^2}{2 \nu_{ii}}, \tag{13}$$

where the factor of three arises because ν_{ii} is a 3-dimensional velocity diffusion rate, whereas the parallel collision rate is one-dimensional. Thus the confinement time is given by

$$t_{\parallel D} = \frac{(L_\parallel/2)^2}{D_\parallel} = \frac{L_\parallel^2 \nu_{ii}}{6 v_{thi}^2} \tag{14}$$

$$= 4.0 \times 10^{-20} n_j \lambda L_\parallel^2 \mu_j^{1/2} T_i^{-5/2}. \tag{15}$$

For PMFX* parameters, $t_{\parallel D}$ is approximately 32 ms, while for PMFX-U it is 2.1 ms, due to the higher T_i. These timescales are a factor of 10^5 and 10^3 higher, respectively, than the multi-bounce estimates predict. PMFX-LD is by far the closest to the multi-bounce regime, but still has $t_{\parallel D} = 0.97$ ms, a factor of 40 greater than the multi-bounce prediction.

C. Implications for throughput

The parallel throughput R, absent radial losses, is given approximately by

$$R = \frac{\pi C L_\perp^2 L_\parallel n_i}{t_p}, \tag{16}$$

where here n_i refers to the density of ions of all species present, and C is the ratio of the separating volume (i.e. the volume between the green and blue cylinders in Fig. 3) to a cylinder of radius $L_\perp$ and length $L_\parallel$. For instance, for the annular region $\frac{1}{2}L_\perp < r < \frac{3}{2}L_\perp$, $C \approx 2$.

We can write this rate in our two different regimes:

$$R = \begin{cases} \pi C L_\perp^2 L_\parallel n_i \nu_{ii} & \text{if } \nu_{ii} L_\parallel / v_{thi} \ll 1 \\ \pi C L_\perp^2 L_\parallel n_i \nu_{ii}^{-1} \left(\frac{6 v_{thi}^2}{L_\parallel^2}\right) & \text{if } \nu_{ii} L_\parallel / v_{thi} \gg 1. \end{cases} \tag{17}$$

Notice that because $\nu_{ii} \propto n_i$, **the throughput rate of the mass filter does not increase with density if** $\nu_{ii} L_\parallel / v_{thi} \gg 1$, i.e. if it is no longer in the multi-bounce regime. Up to that point, however, it increases with n_i^2.

The theoretical optimal scale of the device will be given by operating at the boundary of the multi-bounce regime:

$$L_\parallel = v_{thi} \nu_{ii}^{-1} = \rho \tau_M. \tag{18}$$

Since τ_M is unlikely to be much greater than $\mathcal{O}(10)$ for the accessible temperatures, densities, and magnetic fields, this represents an impractically small device; for instance, on PMFX-U, it would be around 1 cm. Thus in practice we are likely to be in the diffusive parallel transport regime, on which the remainder of the paper will focus.

VII. RADIAL TRANSPORT TIMESCALES

Now that we have established the parallel (axial) transport timescales, we turn our attention to radial transport timescales. We will be primarily concerned with the effects of ion-ion and ion-neutral collisions, neglecting turbulent effects beyond a simple estimate of Bohm diffusion. However, these simple estimates will allow us to define dimensionless parameters τ which will straightforwardly constrain the parameter space for feasible mass filter operation. Note that the analysis throughout this section relies on the assumption that $\tau_M > 1$; if $\tau_M < 1$, the motion is simply mean-free-path scale diffusion.

A. Ion-ion diffusive transport

In considering the trajectory of a minority ion traversing the mass filter, collisions with majority ions will lead to much greater velocity-space diffusion than collisions with electrons. The typical time step will then be the collision time ν_{ii}^{-1}, and the typical step size the gyroradius:

$$\rho_i = 1.0 \times 10^2 \mu_i^{1/2} T_i^{1/2} B^{-1}. \tag{19}$$

The diffusion coeffient (in cm^2/s) is then given by

$$D_{ii} = \frac{1}{2}\rho^2 \nu_{ii} = 1.2 \times 10^{-3} \lambda \mu_j^{1/2} T_i^{-1/2} B^{-2} n_j. \tag{20}$$

The Coulomb confinement time is then given by

$$t_c \sim (L_\perp/2)^2/D \sim 2.2 \times 10^2 \lambda^{-1} B^2 L_\parallel^2 a^2 T_i^{1/2} \mu_j^{-1/2} n_j^{-1}. \tag{21}$$

We can normalize our Coulomb confinement time to our PMF parallel confinement time, giving

$$\tau_c = 5.4 \times 10^{21} B^2 T_i^3 \lambda^{-2} \mu_j^{-1} n_j^{-2} \left(\frac{L_\perp}{L_\parallel}\right)^2. \tag{22}$$

The previous analysis only applies when $\tau_M > 1$. When $\tau_M < 1$, we simply have a collisional diffusion process, and so the ratio of the perpendicular and parallel confinement times is simply the ratio of the square of the distances.

Putting this all together, and rewriting equation (22) in terms of τ_M, we thus have:

$$\tau_c = \begin{cases} \left(\frac{L_\perp}{L_\parallel}\right)^2 & \text{if } \tau_M < 1 \\ 1.4 \left(\frac{L_\perp}{L_\parallel}\right)^2 \tau_M^2 & \text{if } \tau_M > 1. \end{cases} \tag{23}$$

For PMF operation with minimal radial losses, we will need $\tau_c > 1$. As magnetization τ_M becomes greater, this becomes much easier, since τ_c scales with the τ_M^2. On PMFX-U, we have $\tau_c = 12$, and on PMFX-LD, $\tau_c = 10$.

B. Ion-neutral advective transport

If there is relative bulk flow between the ions and neutrals, there will be a net momentum transport that will lead to an $F \times B$ drift, which will tend to push the ions out radially.

To get a simple estimate of the radial drift velocity, we assume that the neutrals are cold and at rest in the lab frame. "Capture" events then occur at the rate given by Eq. (3), and each of these on average transfers momentum $\Delta p = m_p \mu_R v_{E\times B}$, where

$$v_{E\times B} = \frac{cE_{sv}}{B} = 10^8 \frac{E}{B}, \tag{24}$$

where the second equality switches from the Gaussian unit of statvolts/cm (and hence subscripted sv) to the more common experimental unit of volts/cm. So the net force is

$$F_{\text{net}} = P_{in} \Delta p = 8.99 \times 10^{-10} m_p \left(\alpha_R \mu_R\right)^{1/2} n_n v_{E\times B}. \tag{25}$$

This leads to a radial drift with magnitude

$$v_{r,n} = \frac{cF_{\text{net}}}{qB} = 9.4 \times 10^{-6} E \alpha_R^{1/2} \mu_R^{1/2} n_n B^{-2}. \tag{26}$$

The direction of the drift always leads to lower electrical potential energy. To see this result, consider that the direction of the neutral flow in the gyrocenter rest frame points towards $-\mathbf{E} \times \mathbf{B}$. Thus the drift points in the direction $\text{sgn}(q)(-\mathbf{E} \times \mathbf{B}) \times \mathbf{B} = \text{sgn}(q)\mathbf{E}_\perp$.

Once we have the drift velocity, the confinement time is given by

$$t_n = \frac{L_\perp/2}{v_{rn}} = 5.3 \times 10^4 L_\perp E^{-1} \alpha_R^{-1/2} \mu_R^{-1/2} n_n^{-1} B^2 \tag{27}$$

Normalizing by the PMF time:

$$\tau_n = 1.3 \times 10^{24} \frac{B^2 T_i^{5/2}}{E \lambda \alpha_R^{1/2} \mu_R^{1/2} \mu_j^{1/2} n_j n_n} \frac{L_\perp}{L_\parallel^2}. \tag{28}$$

Again, we can write this in terms of τ_M:

$$\tau_n = \begin{cases} \left(\frac{L_\perp}{L_\parallel}\right)^2 & \text{if } \tau_M < 1. \\ 344 \frac{\lambda \mu_j^{1/2}}{E \alpha_R^{1/2} \mu_R^{1/2} T_i^{1/2}} \left(\frac{L_\perp}{L_\parallel^2}\right) \left(\frac{n_j}{n_n}\right) \tau_M^2. & \text{if } \tau_M > 1. \end{cases} \tag{29}$$

This, however, is not the most enlightening result. We would like to know when we should expect motion due to ion-neutral collisions to be dominant. The ratio of the ion-neutral to ion-ion confinement times is

$$\frac{\tau_n}{\tau_c} = 245 \frac{\lambda \mu_j^{1/2}}{E \alpha_R^{1/2} \mu_R^{1/2} T_i^{1/2}} \left(\frac{1}{L_\perp}\right) \left(\frac{n_j}{n_n}\right). \tag{30}$$

We can rewrite this in terms of the relative magnitudes of ion-ion and ion-neutral collisions using equation (6):

$$\frac{\tau_n}{\tau_c} = 9.4 \times 10^{-1} \frac{\nu_{ii}}{\nu_{in}} \frac{\mu_j^{1/2} T_i}{E \alpha_R^{1/2} \mu_R^{1/2}} \left(\frac{1}{L_\perp}\right). \tag{31}$$

Now if the radial electric field arises from a sheath potential at the plasma edge, we have $E \approx 6T_e/L_\perp$. If we further take $\mu_R \approx \mu_j$, then we find

$$\frac{\tau_n}{\tau_c} = \frac{5.6}{\alpha_R^{1/2}} \frac{\nu_{ii}}{\nu_{in}} \left(\frac{T_i}{T_e}\right). \tag{32}$$

Thus, even if the ion-ion collision frequency is a factor of 5 or 10 higher than the ion-neutral collision frequency, the high relative electron temperature in helicon plasmas (where T_e is typically on the order of 5 eV) makes ion-neutral collisions likely to contribute substantially to transport.

On PMFX-U, where we assume a comparatively large electric field of 5 V/cm, $\tau_n = 8.1$. On PMFX-LD, with a smaller magnetic field, $\tau_n = 4.8$

C. Overall confinement times

The overall confinement time is given approximately by

$$t_{\text{conf},D} = \frac{1}{1/t_{\parallel D} + 1/t_c + 1/t_n} = \frac{t_{\parallel D}}{1 + \tau_c^{-1} + \tau_n^{-1}}. \tag{33}$$

When the plasma enters the multi-bounce regime, we expect the confinement time to scale as the collision timescale

$$t_{\text{conf,MB}} \equiv \min\left(\nu_{ii}^{-1}, \nu_{in}^{-1}\right). \tag{34}$$

The transition between these two regimes can be observed in the full MCMF simulations, which probed higher temperatures, as discussed below. Most prior[2,5] studies worked in the temperature range $T_i \geq 10$ eV and density range $n_j \leq 3 \times 10^{12}$ cm^{-3}, on the edge or in the multi-bounce regime.

	Description	Section
τ_M	Gyrocenter drift condition	V
τ_c	Coulomb (ion-ion) collisions	VII A
τ_n	Ion-neutral collisions	VII B
τ_B	Bohm diffusion	VII D

TABLE III. Summary of τ parameters. Effective PMF operation requires all τ's be greater than 1. The latter three τ's are ratios of perpendicular to parallel confinement times, whereas $\tau_M > 1$ ensures gyrocenter drift motion.

	PMFX*	PMFX-U	PMFX-LD
v_{thi} (cm/s)	1.1×10^5	1.9×10^5	1.1×10^5
t_{pD} (s)	3.2×10^{-2}	2.1×10^{-3}	9.7×10^{-4}
ρ_i (cm)	0.94	0.10	0.36
$v_{E\times B}$ (cm/s)	2.1×10^5	3.3×10^4	2.0×10^5
Ω_i (s^{-1})	1.1×10^5	1.8×10^6	3.0×10^5
ν_{ii} (s^{-1})	1.5×10^6	2.8×10^5	4.4×10^4
ν_{in} (s^{-1})	2.9×10^4	2.9×10^4	2.9×10^4
τ_M	0.12	9.6	10
τ_c	4.0×10^{-2}	12	13
τ_n	"	8.1	4.8
τ_B	1.5×10^{-2}	8.3	3.0

TABLE IV. Calculated collision frequencies, τ parameters, and associated important quantities for PMFX*, PMFX-U, and PMFX-LD.

D. Bohm diffusion

A detailed study of the possible effects of turbulence on PMF operation is outside of the scope of this paper, but we will review the most basic turbulence model to get a rough sense of turbulence-induced transport.

The Bohm diffusion coefficient, empirically discovered and believed to arise from randomly fluctuating electric fields, is given by

$$D_B = 6.25 \times 10^6 T_e B^{-1} \mathrm{cm}^2/\mathrm{s}. \tag{35}$$

This will result in a turbulent confinement time

$$t_B = \frac{(L_\perp/2)^2}{D_B} = 4.0 \times 10^{-8} L_\perp^2 B T_e^{-1}. \tag{36}$$

Normalizing by the parallel confinement time, this becomes

$$\tau_B = 1.0 \times 10^{12} \frac{B T_i^{5/2} L_\perp^2}{\lambda \mu_j^{1/2} T_e n_j L_\parallel^2}. \tag{37}$$

Or, in terms of τ_M:

$$\tau_B = 16 \left(\frac{T_i}{T_e}\right) \left(\frac{L_\perp}{L_\parallel}\right)^2 \tau_M. \tag{38}$$

This becomes dominant as we go to higher and higher magnetizations, since it scales linearly (rather than quadratically) with τ_M, in contrast to the other diffusion coefficients. On PMFX-U, we have $\tau_B = 8.3$, and on PMFX-LD, we have $\tau_B = 3.0$.

The meanings of the different τ's are reviewed in table III. Table IV shows values of τ and several associated parameters for PMFX*, PMFX-U, and PMFX-LD.

E. Comparison to Simulations in an Ideal Geometry

To test our τ parameters, we performed single-particle simulations for an annular plasma similar to that shown in Figure 3, but without end mirror fields. For the purpose of the simulations, we took the inner radius of the annulus to be $L_\perp/2$. Particles were initialized with a random, isotropically-distributed thermal velocity in the rotating frame, at $(r, z) = (L_\perp, 0)$. They were considered radially lost if they reached $|r - L_\perp| > L_\perp/2$, and axially

lost if they reached $|z-0| > L_\parallel/2$. We used a nonlinear fourth-order Runge-Kutta particle pusher[11] to advance the Lorentz force. For ion-ion collisions, we employed a Langevin collision model[12] for ion-ion collisions. We had to modify this model (originally formulated for electron-ion collisions) to asymptotically match the formulary collision frequencies and to conserve momentum–this required replacing the background ion mass with the reduced mass in the Maxwellian. Finally, we implemented a Monte Carlo COM scattering model[13] for neutral collisions. We fit the constants in the ion-neutral scattering model to experimentally-obtained ion-neutral collision frequency, given approximately by:[25]

$$P_n = n_n v_i \left(18.1 + 37.7\epsilon_i^{-1/2}\right) \times 10^{-16}, \tag{39}$$

where v_i is the particle velocity and ϵ_i its energy.

Figure 4a shows the results of simulations across a wide range of B, T_i, n_j, and n_n. At $\min(\tau_c, \tau_n) > 1$, almost all particles exit the device axially, while for $\min(\tau_c, \tau_n) < 1$, large numbers of radial exits occur, as expected. Thus, at least in the absence of tubulence, τ_c and τ_n provide a sensible lower bound on the parameter range for mass filter function.

Meanwhile, figure 4b shows the comparison between the predicted (Eq. 33) and simulated diffusive confinement time. Because the plasma in these simulations is firmly in the diffusive parallel transport regime, the agreement is fairly good.

VIII. SPECIAL-CASE τ MODIFICATIONS

In certain cases, particularly at high temperatures, some of our assumptions can break down. However, most of the resulting errors can be easily corrected, as we now discuss.

A. Neutral-collision dominance at high ion temperatures

At high temperatures, the inequality (7) may not hold, meaning that neutral collisions will be dominant in determining the parallel transport timescale $t_\parallel$. Thus we should multiply the parallel confinement time $t_{\parallel D}$ by a factor of ν_{in}/ν_{ii}:

$$t_{\parallel D} \to t_{\parallel D} \max\left(1, \frac{n_n}{n_j}\frac{\alpha_R^{1/2} T_i^{3/2}}{260\lambda}\right) \tag{40}$$

This would in turn multiply both τ_c and τ_n by a factor of ν_{ii}/ν_{in}. Thus

$$\tau_{\substack{c\\n}} \to \tau_{\substack{c\\n}} \min\left(1, \frac{n_j}{n_n}\frac{260\lambda}{\alpha_R^{1/2} T_i^{3/2}}\right). \tag{41}$$

This correction will be significant below, when we consider parameter ranges similar to previous work on MCMF's, which assumed very high ion temperature.

B. Ion-neutral correction at high ion temperatures

If T_i becomes large (as we will soon define), then the polarization scattering calculation will underestimate the ion-neutral collision frequency, since the collision cross section asymptotically approaches a value $\sigma_{in,\min} \sim 2\times10^{-15}$ cm$^2 > 0$. Thus the high-temperature ion-neutral collision frequency becomes

$$P_{in,hT} = \sigma_{in,\min} v_{thi} n_n = 1.1\times10^{15}\sigma_{in,\min}\left(\frac{\mu_R T_i}{\alpha_R \mu_i}\right)^{1/2} P_{in}, \tag{42}$$

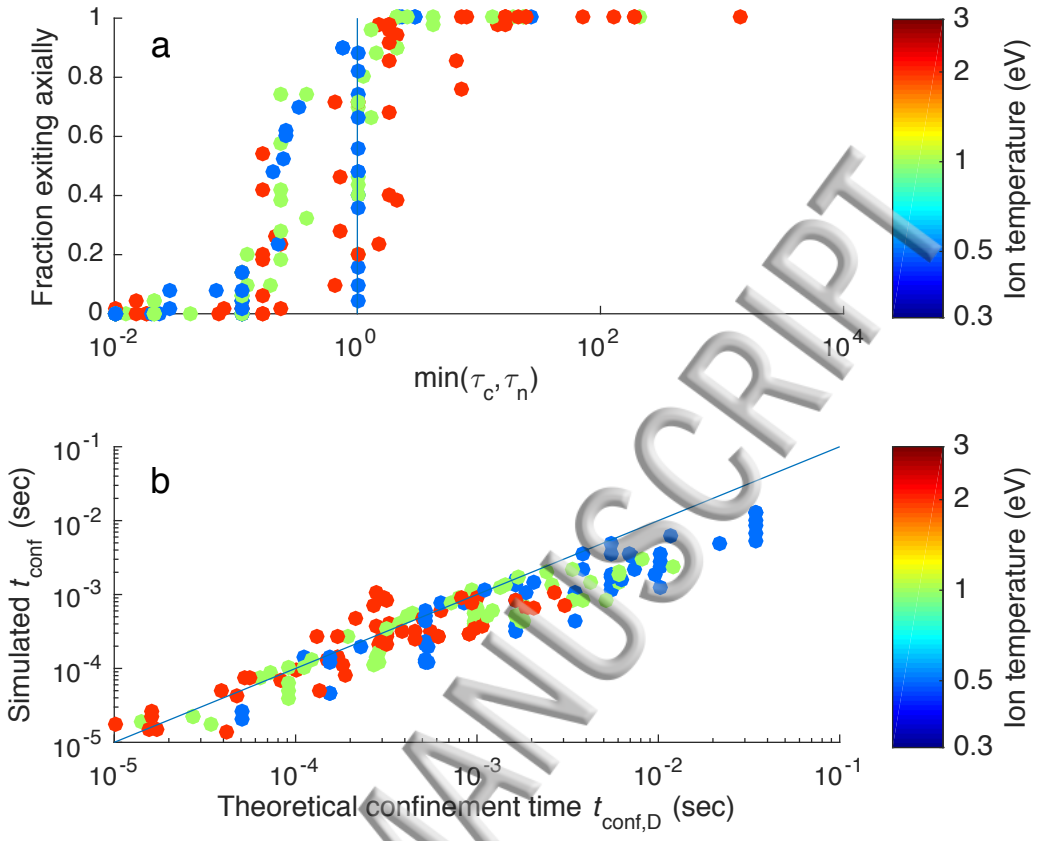

FIG. 4. (a) Dependence of axial (as opposed to radial) exit percentage on normalized perpendicular transport timescales τ_c and τ_n, for several sets of parameters. (b) Comparison of theoretically predicted (Eq. 33) and simulated confinement times. All simulations share $L_\parallel = 30$ cm, $T_e = 5$ eV, $\mu_i = 80$, $\mu_j = 40$, and $E_r = 2$ V/cm. Simulations vary T_i (0.5, 1, and 2 eV), n_e (1×10^{12}, 3×10^{12}, and 1×10^{13} cm^{-3}), n_n (1×10^{13} and 2×10^{14} cm^{-3}), B (1×10^3, 3×10^3, and 1×10^4 G), and $L_\perp$ (3, 10, and 30 cm). Percentages are based on 50 trials per parameter set. Only a few parameter sets with $T_i \leq 1$ eV manage to avoid massive numbers of radial exits; those which do correspond to parameter sets at the lowest ion and neutral densities.

Thus, when the prefactor on the RHS of the above equation becomes much greater than one–which will occur at high temperatures–we will need to switch to the hard-sphere scattering model, reducing τ_n. For instance, in the approximately empirical cross section of Eq. (39), this transition occurs at $T_i \sim 4$ eV. We can easily incorporate this correction by letting

$$\tau_n \to \tau_n \min\left(1, \frac{\nu_{in}}{\nu_{in,hT}}\right). \tag{43}$$

where the collisionality ratio is defined in equation (42).

Note that this calculation in turn implies

$$\nu_{in,hT} = 1.1 \times 10^{15} \sigma_{in,\min} \left(\frac{\mu_R T_i}{\alpha_R \mu_i}\right)^{1/2} \frac{\nu_{in}}{\nu_{ii}} \nu_{ii} \tag{44}$$

$$= 4.2 \times 10^{12} \sigma_{in,\min} \left(\frac{\mu_j}{\mu_i}\right)^{1/2} \left(\frac{n_n}{n_j}\right) \frac{T_i^2}{\lambda} \nu_{ii}. \tag{45}$$

We can thus now include the case where parallel transport is dominated by hard-sphere (rather than polarization) scattering off neutrals. Thus the generalization of Eq. (41) to

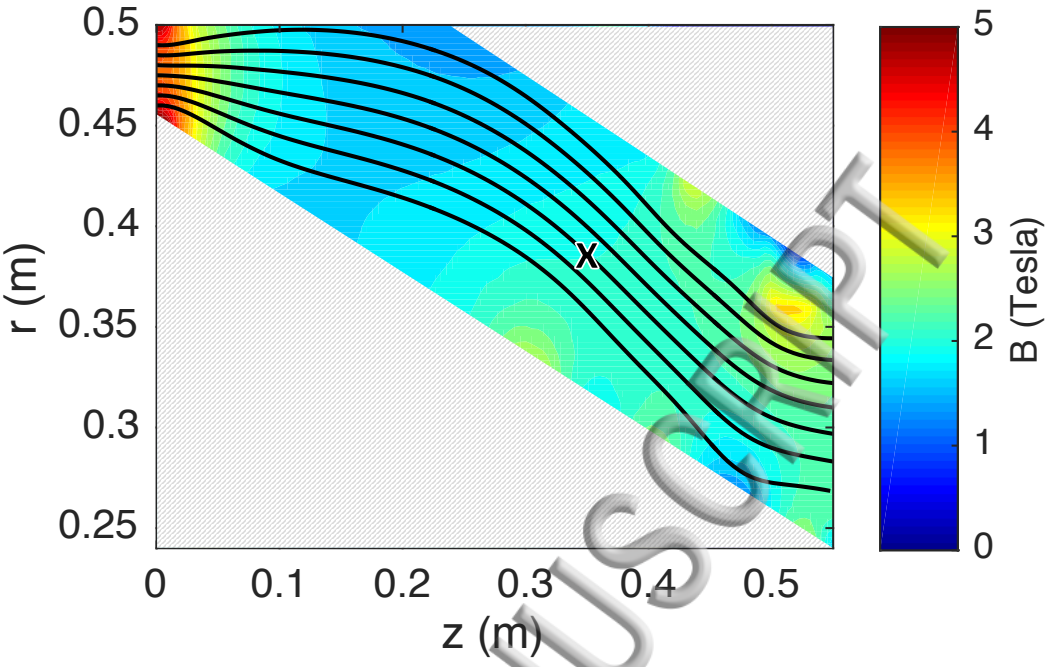

FIG. 5. Magnetic field configuration from Gueroult and Fisch [2], optimized for separating lanthanides (∼ 144 a.m.u.) from actinides (∼ 241 a.m.u.). Electric field is derived by taking streamlines (shown in black) as equipotential surfaces. The injection point for ions in the simulation is marked with a black x.

hard-sphere neutral scattering, wherein we include a factor of $\nu_{ii}/\nu_{in,hT}$ is

$$\tau_{\substack{c\\n}} \rightarrow \tau_{\substack{c\\n}} \min\left(1, \frac{n_j}{n_n}\frac{260\lambda}{\alpha_R^{1/2}T_i^{3/2}}, \frac{2.3\times10^{-13}}{\sigma_{in,\min}}\frac{\mu_i^{1/2}n_j\lambda}{\mu_j^{1/2}n_nT_i^2}\right). \tag{46}$$

Applying Eq.'s (43) and (46) corrects most overly optimistic predictions of the model.

C. Multi-bounce regime

Finally, it should be mentioned that it is always worth checking whether the mass filter is operating in the multi-bounce regime. If so, it is highly unlikely that radial exits will be significant, since the collision time will also be the characteristic exit time, making significant radial diffusion impossible. Fortunately, if the bounce time is longer than the collision time, our calculations of τ_c and τ_n are almost certain to yield values much greater than one, so there is no real benefit to adjusting the τ's to account for this case.

IX. SIMULATIONS FOR PREVIOUSLY PROPOSED MCMF CONFIGURATION

Now that we have performed simulations in an idealized geometry, we can move on to a more realistic plasma mass filter configuration. In this section, we make use of a magnetic field configuration (Figure 5) previously studied[2] in numerical simulations and optimized for separating lanthanides (∼ 144 a.m.u.) from actinides (∼ 241 a.m.u.), and test across a range of ion and neutral densities and temperatures. The simulated magnetic field in that work ranged from about $B \approx 1.5\times10^4$ G at the center, to $B \approx 5\times10^4$ G at the mirror,

with $E \approx 60$ V/cm at the injection point, which we took to be at $r = 38$ cm, $z = 35$ cm (marked with a black x in the figure) in agreement with the earlier study.

In performing the parameter sweep, we adjusted the electric field so that $E \propto \sqrt{T_i}$ between parameter sets. This constraint ensured that the loss cones had the same shape across each simulation, since the centrifugal energy W_{cent} scales as $W_{\text{cent}} \propto v_{E\times B}^2 \propto E^2$, and we want $W_{\text{cent}} \sim T_i$. As in the previous study, we considered particles initialized at rest in the lab frame.

Results of simulations for this configuration are shown in Figure 6. Parameter sets which are similar to those used in the original numerical study[2] are shown as open circles, whereas other parameter sets are shown as filled circles. We found that to reproduce the results of the earlier paper in terms of separations at $T_i = 20$ eV, we had to reduce the electric field by a factor of four, to $E \approx 15$ V/cm. Thus, consistently between parameter sets, we maintained $E \approx 15\sqrt{T_i/20}$ V/cm at the injection point.

The results for axial vs. radial exiting are largely comparable to those for the idealized MCMF, except for the divergence at large T_i and n_n, where a failure to account for the transition from ion- to neutral-dominated collisions at high temperatures results in overly optimistic projections for τ_c and τ_n. This discrepancy can be seen by comparing the small red diamonds, representing $T_i = 20$ ions at large neutral ($n_i > 10^{19}$) densities, in the three panels of Figure 6. Figure 6a applies the analysis of Section VII directly, while 6b-c apply the corrections from Sections VIII A and VIII B respectively. In Figure 6a, some parameter sets have a $\min(\tau_c, \tau_n) > 10$, despite experiencing large numbers of radial exits, while in Figure 6b these values are corrected to be much closer to 1 in accordance with Eq. (41). This correction accounts for the fact that the axial exit time is determined by ion-neutral, rather than ion-ion, collisions at high temperatures. When we additionally factor in the hard-sphere scattering cross section of ion-neutral collisions at high temperatures (Eqs. 43 and 46), we find that all parameter sets with large numbers of radial exits have $\min(\tau_c, \tau_n)$ less than 1, as desired. Thus it is important, especially in hot plasmas with high neutral densities, to double check that none of the conditions in Section VIII apply before calculating τ_c and τ_n directly from Section VII.

We also can observe the transition between diffusive and multi-bounce exit behavior in Figure 7a-b. At low temperatures, the exit time agrees well with the diffusive model, while at high temperatures the multi-bounce exit time is a better predictor.

Finally, in Figure 8, we actually evaluate the separation for each parameter set, considering the fraction of both light and heavy particles (given that they exit axially) that exit on on the left (heavy boundary) side of the device. We can see that there is a temperature dependence, perhaps resulting from the modification of the electric field with temperature, which results in more particles exiting at the heavy boundary as the temperature increases. The fraction of particles exiting at the heavy boundary also increases with τ_n. Finally, the separation factor data is somewhat noisy, perhaps resulting from the relatively low number of trials.

X. DISCUSSION

Now that we have established several dimensionless parameters and confinement time scalings, it is time to examine their implications for device design. In this section, we will start by taking a second look at neutrals, examining the applicability regime of some of our underlying assumptions in modeling them. Then, we will look at how the presence of neutrals combines with other constraints to reduce the favorable scaling of the τ's above certain threshold ion temperatures, fundamentally limiting the operating regime of a real device. We will then provide rough estimates for the throughput of a realistic mass filter, defining favorable operating points for an initial proof-of-concept experiment, as well as a prototype industrial separator.

A. Neutral rotation profile

The advective transport calculation assumed that neutrals were on average at rest in the lab frame. However, if the device is sufficiently large and the plasma sufficiently dense, the ion-neutral momentum coupling can be strong in certain regions of the plasma, eliminating the relative flow that gives rise to the advective effect. Thus the penetration distance of the advective effect should be given approximately by

$$L_n = \lambda_{\text{mfp}} = v_{thn}/K_L n_j = 1.1 \times 10^{15} n_j^{-1} \left(\frac{\mu_R T_n}{\alpha_r \mu_j} \right)^{1/2}. \tag{47}$$

For room-temperature thermal ($T_n = 0.026$ eV) Argon atom collisions with Argon ions at a density of $n_j = 10^{13}$ cm^{-3}, we have $L_n = 4.3$ cm $\sim L_\perp$, so advective effects should be significant; and would be even more significant if the neutrals were heated significantly above room temperature. However, for larger or denser filters, advection could be suppressed at the core by this mechanism.

B. Constrained scaling of τ_n

We know from Eq. (28) that $\tau_n \propto T_i^{5/2}$. However, this scaling assumes that we can set E and T_i independently. It may be more natural to constrain ourselves, as we did in the MCMF simulations, to hold $v_{E\times B}^2/T_i$ constant, thus maintaining the shape of the loss cone. Because $v_{E\times B} \propto E/B$, this will make $\tau_n \propto T_i^2$, slightly reducing the favorable scaling with temperature.

It is instructive to consider the full range of scaling with temperature. At first, when ion-ion collisions dominate, we have $\tau_n \propto T_i^2$, $\tau_c \propto T_i^3$. When the temperature high enough that neutral collisions are dominant, the scaling will degrade to $\tau_n \propto T_i^{1/2}$, and $\tau_c \propto T_i^{3/2}$ (Eq. 41). When the temperature becomes high enough that the ion-neutral scattering transitions from the polarization regime to the hard-sphere regime, the scaling will further degrade to $\tau_n \propto T_i^0$, and $\tau_c \propto T_i^1$ (Eq. 46). Thus there will be a limit to the achievable τ_n, which will set fundamental limits on the density and dimensions of the device. For instance, in Figure 6c at high neutral densities (diamond markers), increasing the temperature from 10 to 20 eV does not result in an increase in $\min(\tau_n, \tau_c)$, as can be seen by the clustering of orange and red diamond markers to the left of the line delineating $\min(\tau_n, \tau_c) = 1$. However, this fundamental limit should only occur at $T_i \gtrsim 10$ eV, as long as the device does not have $L_\perp \ll L_\parallel$. Thus technological and radiative limitations are likely to constrain the ion temperature below the point where this degradation of favorable scaling is observed.

C. Throughput

Without considering potential degradiation in separation efficiency, the maximum throughput (in gm/s) once all parameters other than ion density are specified is given by (see Section VI C):

$$R = 6\pi C L_\perp^2 \langle m_p \mu_i \rangle \tilde{\nu}_{ii}^{-1} v_{thi}^2 L_\parallel^{-1}, \tag{48}$$

where $\tilde{\nu}_{ii} \equiv \nu_{ii}/n_i$, and we have assumed we can make $\nu_{in} < \nu_{ii}$. Now let $\epsilon = L_\perp/L_\parallel$, where we are imagining that the mass filter function depends on a fixed geometry. Then

$$R = 6\pi C L_\parallel \epsilon^2 \tilde{\nu}_{ii}^{-1} v_{thi}^2 \tag{49}$$

$$= 7.9 \times 10^{-4} C \lambda^{-1} \mu_j^{-1/2} \langle \mu_i \rangle \epsilon^2 L_\parallel T_i^{5/2}. \tag{50}$$

This predicts that a device with the parameters of PMFX-U can process about 10 mg/s. However, the $T_i^{5/2}$ scaling means that large throughput gains are possible by pushing to even modestly higher temperatures; a twofold gain in temperature will lead to a five-fold increase in throughput, and a five-fold gain in temperature to throughputs on the order of gm/s.

Much as in the last section, this $T_i^{5/2}$ scaling will only last so long as $\nu_{ii} > \nu_{in}$. When ν_{in} becomes dominant, the throughput will scale as $R \propto v_{thi}^2 \nu_{in}^{-1} \propto T_i$. Then at higher temperatures, hard-sphere ion-neutral scattering will further reduce the scaling to $R \propto T_i^{1/2}$.

Thus the general message is that raising the ion temperature only dramatically improves performance so long as $\nu_{ii} > \nu_{in}$. However, at high ionization fractions, Eq. (7) tells us that we should continue to see strong performance gains up through $T_i \sim 10$ eV.

Figure 9 shows the comparison of maximum throughput according to Eq. (50), taking into account radial exits, i.e. $R \times P(\text{axial exit})$, with simulations. At low ion temperatures ($T_i < 3$ eV), the throughput is near the theoretical maximum. At higher temperatures, the gradual transition to multi-bounce behavior results in lower throughput compared to the theoretical maximum (which occurs in the diffusive parallel transport regime). However, this model does not take into account possible degradation in separation at higher density, which could make it desirable to operate at lower densities.

D. Mass filter operating regime

Given the desire to (a) achieve maximum throughput and (b) minimize collisional radial losses, while (c) avoiding excessive radiation and turbulent diffusion, both of which tend to increase with electron temperature above 1 eV, it is clearly desirable to maintain the plasma in a hot-ion mode, with $T_i \gg T_e$. In general, however, helicon plasmas tend to have electron temperatures well in excess of the ion temperature.[6,7,28] Thus ion heating should be a major goal of any PMF research program.

One promising way to heat the plasma is simply through the imposition of the already-necessary radial electric field, either via concentric endplates, a biased core, or (in steady state) perhaps through wave-induced radial diffusion. In such a system, an ion generated approximately at rest in lab frame would have a velocity of $v_{E\times B}$ in the $\mathbf{E}\times\mathbf{B}$-drifting plasma rest frame, and thus possibly a quite large thermal velocity. The electrons would receive m_e/m_i less energy, a negligible quantity in comparison. Thus in principle it would be possible to maintain $T_i > T_e$. Such a temperature ordering has been observed, for instance, in rotating mirror machines.[24]

However, there are several caveats. First, it is generally difficult and perhaps impossible to maintain a plasma at $v_{E\times B}$ such that $\frac{1}{2}m_i v_{E\times B}^2$ is greater than the ionization energy of the background plasma.[29] While noble gases suitable for early experiments tend to have high ionization energies ($J > 10$ eV), the ionization energies of fission products tend to fall in the 4-7 eV range, resulting in a fairly low upper limit for temperature.

Second, although the ions may be produced at a much higher temperature than the electrons, they will collisionally thermalize over time. If the parallel transit time $t_\parallel$ and radiative cooling time t_{rad} are significantly greater than the thermalization time t_{therm}, then the electron and ion temperatures could be the same.

XI. CONCLUSIONS

By considering an idealized model of a plasma mass filter, we have identified several dimensionless parameters, τ_M, τ_c, τ_n, and τ_B (see Table III), which should be greater than one to ensure that collisions do not destroy effective mass filter functioning. Thus we have provided a simple theory that can explain the radial loss behavior in realistic MCMF simulations. We have shown that the maximum throughput of the plasma mass filter scales

as $T_i^{5/2}$, while the τ parameters associated with maintaining gyro-drift motion and avoiding ion-ion and ion-neutral collisional radial losses scale with $T_i^{3/2}$, T_i^3, and $T_i^{5/2}$ respectively. These scalings persist for $\nu_{ii} > \nu_{in}$, i.e. for $T_i \lesssim 10$ eV. Since both radiated energy and turbulent transport are expected to increase with the electron temperature, we conclude that it is highly desirable to operate in a hot-ion mode, although the ability to do this may be limited by the critical ionization velocity and electron-ion thermalization.

Thus a major conclusion of this work is the importance of ion heating for gyro-drift dependent mass filter designs. The low ion temperatures ($T_i \lesssim 1$ eV) typical of helicon plasmas simply are not conducive to either gyro-drift motion or axial collection of ion species at the densities required for high throughput. Therefore demonstrating the feasibility of maintaining high ion temperatures, preferably while keeping electron temperatures low, should become a key component of the mass filter research program.

We have also used the τ parameters to evaluate the design of two potential upgraded mass filter experiments. The first, PMFX-U, aimed to work at comparable densities to the current experiment, and thus required a factor-of-15 increase in the magnetic field and a factor-of-3 increase in the ion temperature over the current experiment[14]. The second reduced collisionality by dramatically reducing the density (by a factor of 30 for ions, and 10 for neutrals), with only a modest increase in the magnetic field. The latter upgrade is probably more technologically feasible in the short term, however it would be fundamentally limited in throughput (Eq. 50). The former would require the development of technologies, particularly for ion heating, likely to be necessary anyway in extrapolating to a prototype high-throughput nuclear waste separator.

Assuming that such ion heating is achievable, the current work suggests that mass filter throughputs on the order of 3 g/s, or 90 metric tons per year, could be achievable by a mass filter around 5 m in length. Since a typical nuclear reactor produces around 20 metric tons of waste each year, such a device could feasibly be used to separate waste on site. For a site such as Hanford, with on the order of 10^4 metric tons of nuclear waste, 10 such devices would take around a decade to clean up the site.

Often, the transport in open-field-line, magnetized, low-temperature plasmas is governed by coherent fluctuations and turbulence.[30–33] However, recent studies have suggested that in heavily magnetized ($B > 1200$ G) open-field-line plasmas, turbulent transport becomes heavily suppressed, in an effect analogous to the formation of a transport barrier in the tokamak L-H transition.[34,35] Thus, although the classical transport calculations here must be regarded as a lower bound on device feasibility, the suppression of turbulent transport at high magnetic field suggests that the classical transport calculations presented could be sufficient constraints on the parameter space for PMF operation.

In order to more fully predict mass filter stability and throughput, including effects such as turbulence, self-consistent neutral rotation and neutral-induced conductivity, and minority ion transport, gyro-two-fluid (or three-fluid, if neutrals are included) simulations should be conducted. These would give more detailed estimates of throughput and separation. In the end, however, only laboratory experiments will be able to elucidate which effects are dominant in determining the efficacy of the device. The estimates in the current paper should provide a good parametric starting point for these experiments.

XII. ACKNOWLEDGMENTS

The authors would like to thank Fred Levinton, Matthew Galante, Matthew Reinke, and Andrei Khodak for useful discussions. This work was supported by DOE contract number DE-AC02-09CH11466. One author (IEO) also acknowledges the support of the DOE Computational Science Graduate Fellowship.

XIII. REFERENCES

[1]R. Gueroult, D. T. Hobbs, and N. J. Fisch, "Plasma filtering techniques for nuclear waste remediation," Journal of hazardous materials **297**, 153–159 (2015).

[2]R. Gueroult and N. Fisch, "Plasma mass filtering for separation of actinides from lanthanides," Plasma Sources Science and Technology **23**, 035002 (2014).

[3]W. E. Parkins, "The uranium bomb, the calutron, and the space-charge problem," Physics Today **58**, 45–51 (2005).

[4]A. V. Timofeev, "On the theory of plasma processing of spent nuclear fuel," Physics-Uspekhi **57**, 990 (2014).

[5]R. Gueroult and N. J. Fisch, "Practical considerations in realizing a magnetic centrifugal mass filter," Physics of Plasmas **19**, 122503 (2012).

[6]D. Leneman, W. Gekelman, and J. Maggs, "The plasma source of the large plasma device at university of california, los angeles," Review of scientific instruments **77**, 015108 (2006).

[7]E. Scime, J. Carr Jr, M. Galante, R. Magee, and R. Hardin, "Ion heating and short wavelength fluctuations in a helicon plasma source," Physics of Plasmas **20**, 032103 (2013).

[8]T. Ohkawa and R. Miller, "Band gap ion mass filter," Physics of Plasmas 9, 5116–5120 (2002).

[9]R. Gueroult, J.-M. Rax, and N. J. Fisch, "The double well mass filter," Physics of Plasmas **21**, 020701 (2014).

[10]A. J. Fetterman and N. J. Fisch, "The magnetic centrifugal mass filter," Physics of Plasmas **18**, 094503 (2011).

[11]J. Berland, C. Bogey, and C. Bailly, "Low-dissipation and low-dispersion fourth-order runge–kutta algorithm," Computers & Fluids **35**, 1459–1463 (2006).

[12]W. M. Manheimer, M. Lampe, and G. Joyce, "Langevin representation of coulomb collisions in pic simulations," Journal of Computational Physics **138**, 563–584 (1997).

[13]C. K. Birdsall, "Particle-in-cell charged-particle simulations, plus monte carlo collisions with neutral atoms, pic-mcc," IEEE Transactions on Plasma Science **19**, 65–85 (1991).

[14]R. Gueroult, E. Evans, S. Zweben, N. Fisch, and F. Levinton, "Initial experimental test of a helicon plasma based mass filter," Plasma Sources Science and Technology **25**, 035024 (2016).

[15]A. Litvak, S. Agnew, F. Anderegg, B. Cluggish, R. Freeman, J. Gilleland, R. Isler, W. Lee, R. Miller, T. Ohkawa, *et al.*, "Archimedes plasma mass filter," in *30th EPS Conference on Contr. Fusion and Plasma Phys*, Vol. 27 (2003).

[16]T. Desjardins and M. Gilmore, "Dynamics of flows, fluctuations, and global instability under electrode biasing in a linear plasma device," Physics of Plasmas **23**, 055710 (2016).

[17]S. Shinohara and S. Horii, "Initial trial of plasma mass separation by crossed electric and magnetic fields," Japanese Journal of Applied Physics **46**, 4276 (2007).

[18]S. Shinohara, N. Matsuoka, and S. Matsuyama, "Establishment of strong velocity shear and plasma density profile modification with associated low frequency fluctuations," Physics of Plasmas (1994-present) **8**, 1154–1158 (2001).

[19]S. Shinohara, N. Matsuoka, and T. Yoshinaka, "Profile control and plasma rotation by biased electrodes in large diameter rf produced plasma," Japanese journal of applied physics **38**, 4321 (1999).

[20]A. Tsushima, T. Mieno, M. Oertl, R. Hatakeyama, and N. Sato, "Control of radial potential profile and nonambipolar ion transport in an electron cyclotron resonance mirror plasma," Physical review letters **56**, 1815 (1986).

[21]A. Tsushima and N. Sato, "Control of radial potential profile by biased segmented endplatesin an ecr plasma," Journal of the Physical Society of Japan **60**, 2665–2672 (1991).

[22]D. A. Schaffner, T. Carter, G. Rossi, D. Guice, J. Maggs, S. Vincena, and B. Friedman, "Modification of turbulent transport with continuous variation of flow shear in the large plasma device," Physical review letters **109**, 135002 (2012).

[23]G. Severn and N. Hershkowitz, "Radial control of the electrostatic potential in a tandem mirror with quadrupole end cells," Physics of Fluids B: Plasma Physics **4**, 3210–3215 (1992).

[24]G. Abdrashitov, A. Beloborodov, V. Volosov, V. Kubarev, Y. S. Popov, and Y. N. Yudin, "Hot roating plasma in the psp-2 experiment," Nuclear Fusion **31**, 1275 (1991).

[25]M. A. Lieberman and A. J. Lichtenberg, *Principles of plasma discharges and materials processing* (John Wiley & Sons, 2005).

[26]R. Comfort, "The magnetic mirror force in plasma fluid models," Modeling magnetospheric plasma , 51–53 (1988).

[27]R. Post, "The magnetic mirror approach to fusion," Nuclear Fusion **27**, 1579 (1987).

[28]M. Gilmore, A. Lynn, T. Desjardins, Y. Zhang, C. Watts, S. Hsu, S. Betts, R. Kelly, and E. Schamiloglu, "The helcat basic plasma science device," Journal of Plasma Physics **81**, 345810104 (2015).

[29]C. Teodorescu, R. Clary, R. Ellis, A. Hassam, R. Lunsford, I. Uzun-Kaymak, and W. Young, "Experimental study on the velocity limits of magnetized rotating plasmas," Physics of Plasmas **15**, 042504 (2008).

[30]M. Burin, G. Tynan, G. Antar, N. Crocker, and C. Holland, "On the transition to drift turbulence in a magnetized plasma column," Physics of Plasmas **12**, 052320 (2005).

[31]A. Light, S. Thakur, C. Brandt, Y. Sechrest, G. Tynan, and T. Munsat, "Direct extraction of coherent mode properties from imaging measurements in a linear plasma column," Physics of Plasmas **20**, 082120 (2013).
[32]S. Thakur, C. Brandt, L. Cui, J. Gosselin, A. Light, and G. Tynan, "Multi-instability plasma dynamics during the route to fully developed turbulence in a helicon plasma," Plasma Sources Science and Technology **23**, 044006 (2014).
[33]C. Brandt, S. Thakur, and G. Tynan, "Investigating flow patterns and related dynamics in multi-instability turbulent plasmas using a three-point cross-phase time delay estimation velocimetry scheme," Physics of Plasmas **23**, 042304 (2016).
[34]L. Cui, A. Ashourvan, S. Thakur, R. Hong, P. Diamond, and G. Tynan, "Spontaneous profile self-organization in a simple realization of drift-wave turbulence," Physics of Plasmas **23**, 055704 (2016).
[35]S. Thakur, J. Gosselin, J. McKee, E. Scime, S. Sears, and G. Tynan, "Development of core ion temperature gradients and edge sheared flows in a helicon plasma device investigated by laser induced fluorescence measurements," Physics of Plasmas **23**, 082112 (2016).

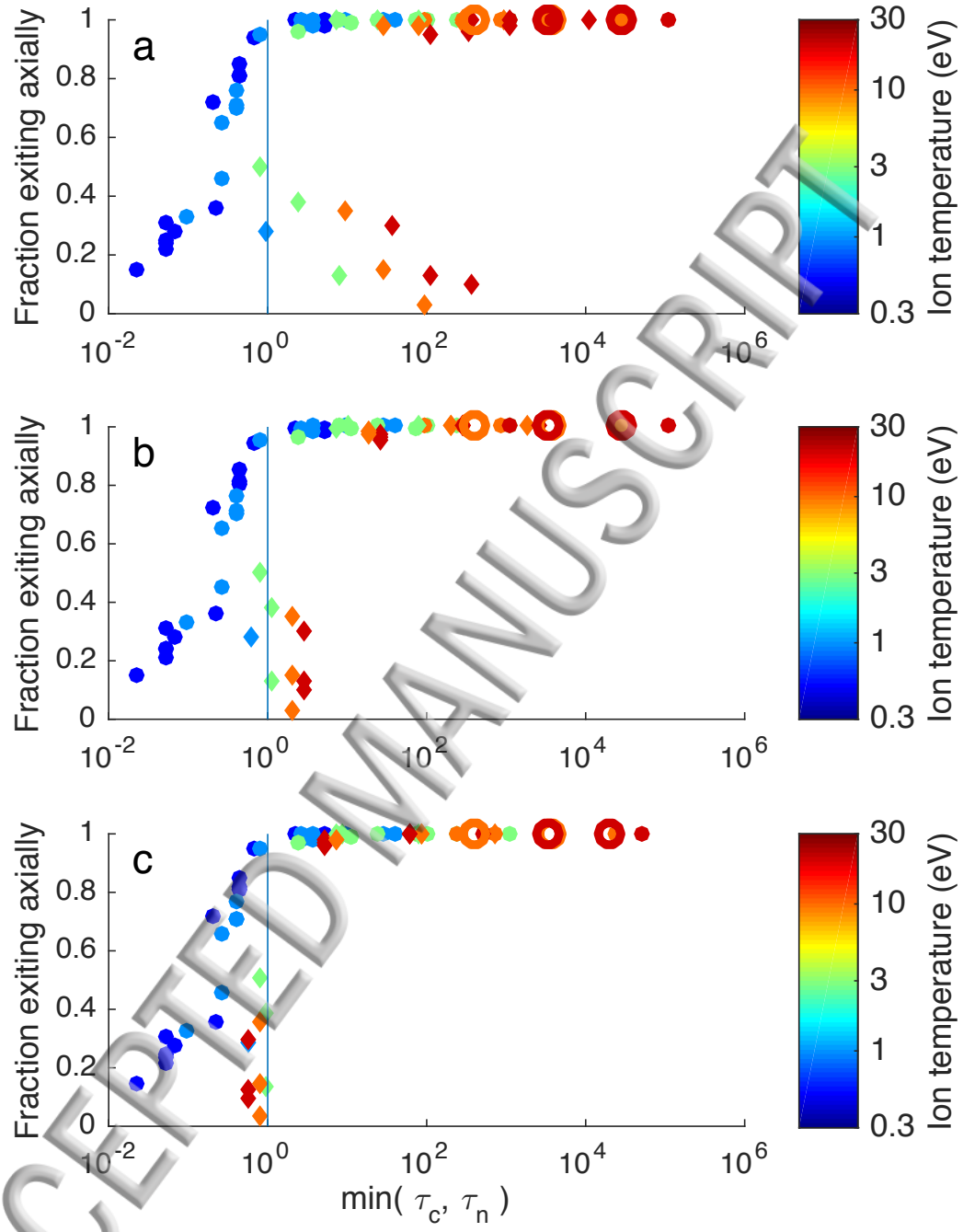

FIG. 6. Dependence of axial (as opposed to radial) exit percentage for realistic MCMF on normalized perpendicular transport timescales τ_c and τ_n, for several sets of parameters. All simulations share $B = 1.5 \times 10^4$ G, $T_e = 5$ eV, $\mu_i = 231$, $\mu_j = 144$, and $v_{E\times B} = 1.0 \times 10^5 \sqrt{T_i/20}$ cm/s at the injection point. Simulations vary T_i (0.5, 1, 3, 10, and 20 eV), n_e (3×10^{11}, 1×10^{12} and 3×10^{12} cm^{-3}), and n_n (1×10^{12}, 1×10^{13}, 3×10^{13}, 1×10^{14}, and 3×10^{14} cm^{-3}). Percentages are based on 200 trials per parameter set. Hollow circles indicate parameter sets close to those considered in earlier studies[2], and diamonds indicate parameter sets for which $\nu_{in} > \nu_{ii}$. Figure (a) ignores all the corrections from Section VIII, (b) incorporates the high-temperature corrections due to neutral collision dominance from Section VIII A (Eq. 41), and (c) further incorporates high-temperature corrections due to hard-sphere ion-neutral scattering from Section VIII B (Eqs. 43 and 46). Thus Figure (a), and to a lesser extent Figure (b), are overly optimistic about some of the high-temperature parameter sets. Incorporating all corrections, however, ensures that $> 90\%$ of ions exit along field lines when $\min(\tau_c, \tau_n) > 1$. Note that, as with the idealized MCMF, few parameter sets with $T_i \leq 1$ eV manage to avoid massive numbers of radial exits.

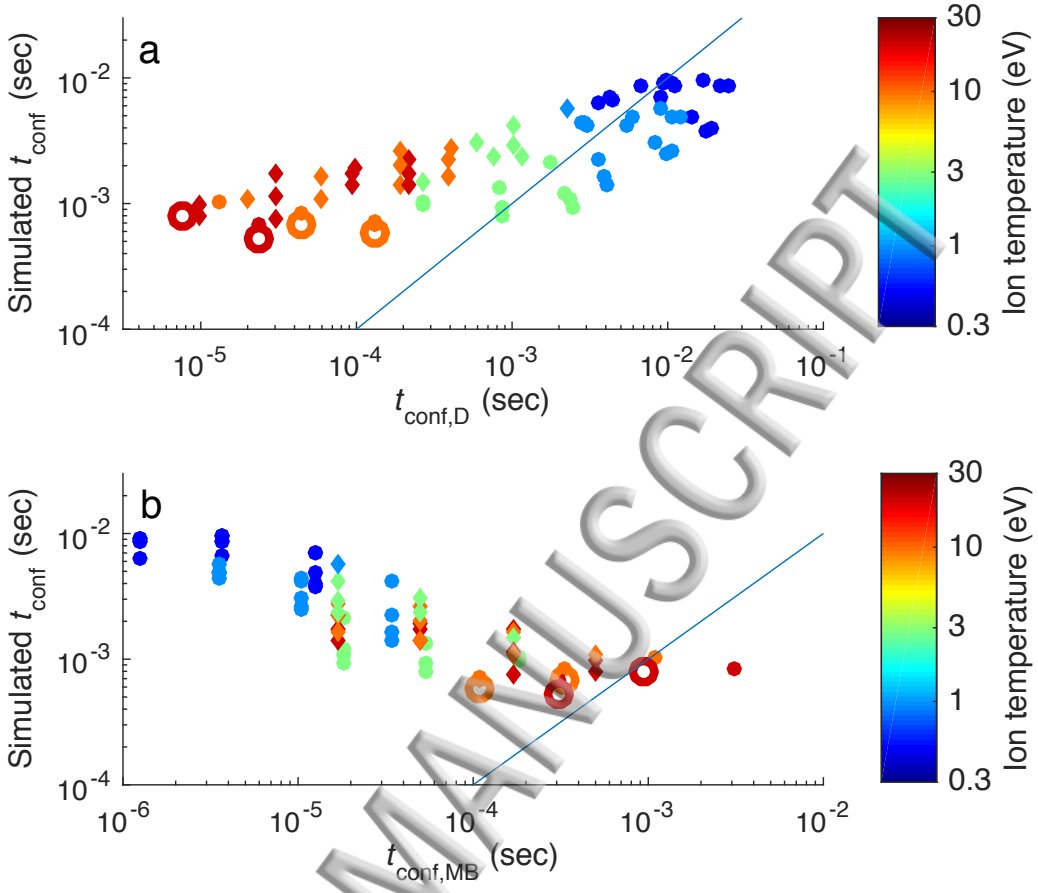

FIG. 7. Predicted vs simulated confinement times for a realistic MCMF, from the same simulation as in Figure 6. Lines in each plot represent perfect agreement between simulation and analytical results. (a) Theoretical confinement times for diffusive parallel transport from Eq. (33). (b) Theoretical confinement times for multi-bounce parallel transport from Eq. (34). Note that the multi-bounce confinement time *increases* with temperture, while the diffusive confinement time *decreases* with temperature. This switch results from the fact that in the multi-bounce regime, greater collisionality (at lower temperature) results in faster scattering into the loss cone, while in the diffusive regime, greater collisionality results in a shorter mean-free path, preventing the particle from diffusing out of the device. Thus as T_i grows large, we enter the multi-bounce regime–and we see from the open circles that prior studies have in general operated in or near this regime.

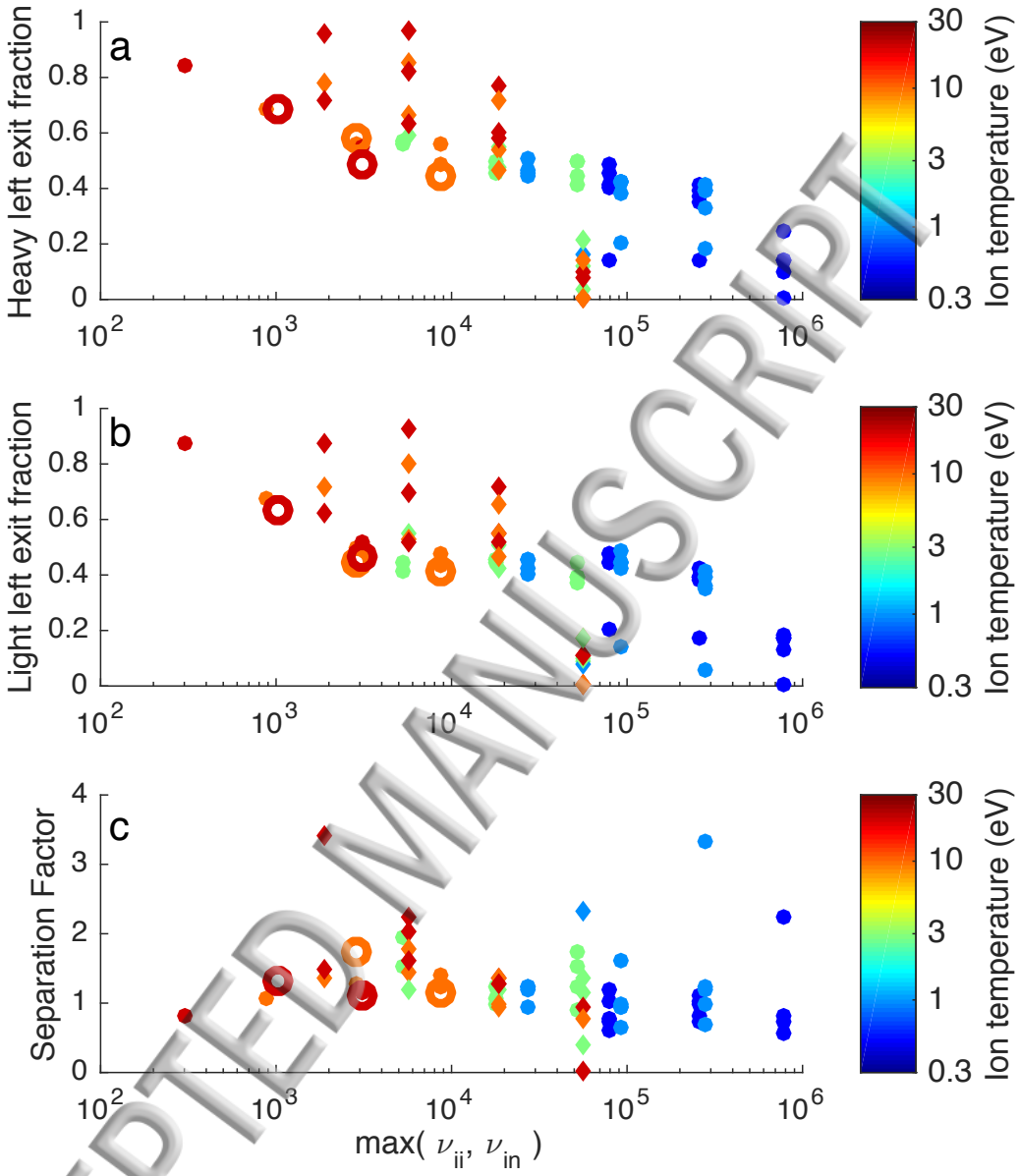

FIG. 8. Which side of the device particles exit from, given that they exit axially, for a realistic MCMF, from the same simulation as in Figure 6. Diamonds indicate parameter sets for which $\nu_{in} > \nu_{ii}$. (a-b) Number of heavy (a) and light (b) ions leaving from the left side (light boundary) of the device as a function of $\max(\nu_{ii}, \nu_{in})$ and temperature. Higher collisionality corresponds to fewer exits from the left (mirror) side of the device. Note that, for intermediate values of the collisionality, neutral-dominated collisions tend to force the ions towards the left exit, consistent with the addition of a radially-directed force. (c) The separation factor, i.e. the ratio of the heavy element fraction on either end of the device, for an initial heavy element ratio of 2% is presented. At low collisionality, the separation ratio varies only slightly with the collisionality, while at high temperatures it varies greatly, likely as a result of the large number of radial exits.

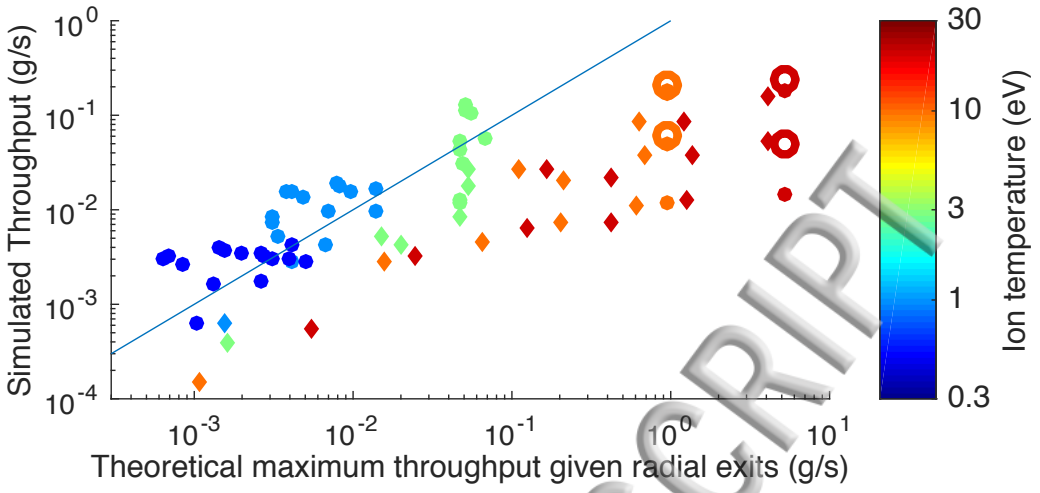

FIG. 9. Simulated throughput (g/s) vs maximum theoretical throughput for MCMF, given the simulated axial exit fraction. At high temperatures, the maximum is not achieved, since the particle is in the multi-bounce regime–however, the separation fraction is better in this regime, making practical throughput higher.

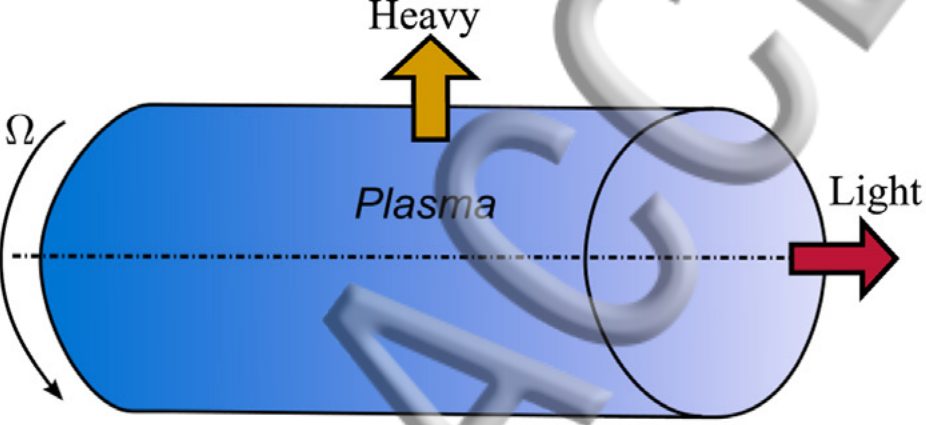

(a) Archimedes Filter

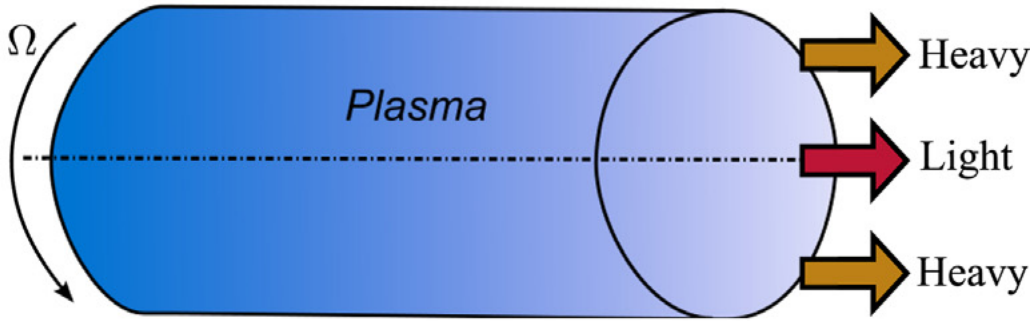

(b) Double Well Filter

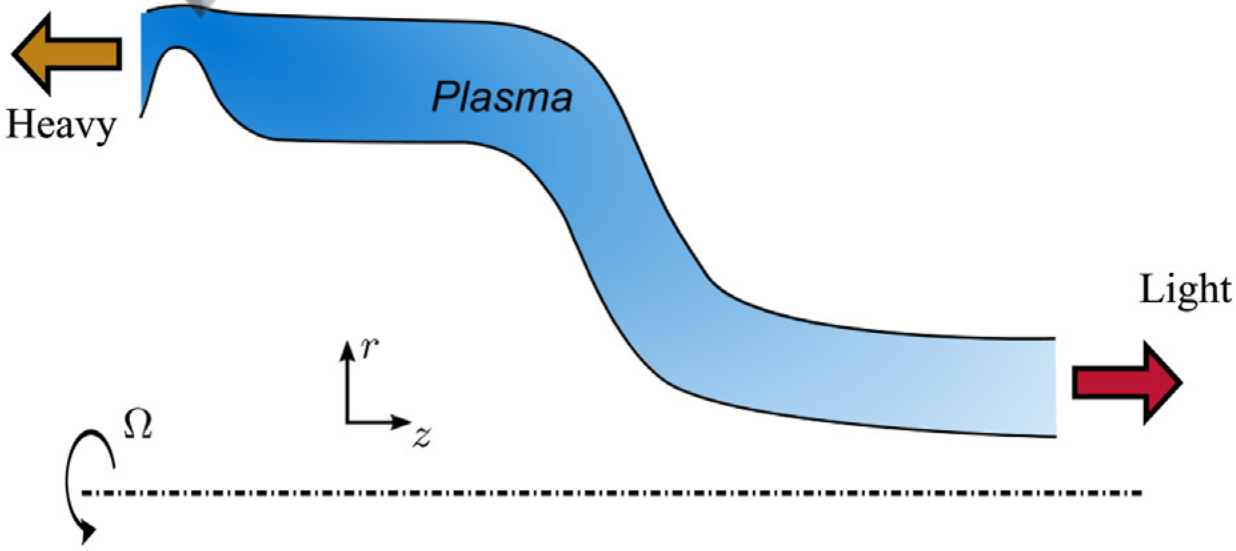

(c) MCMF Filter

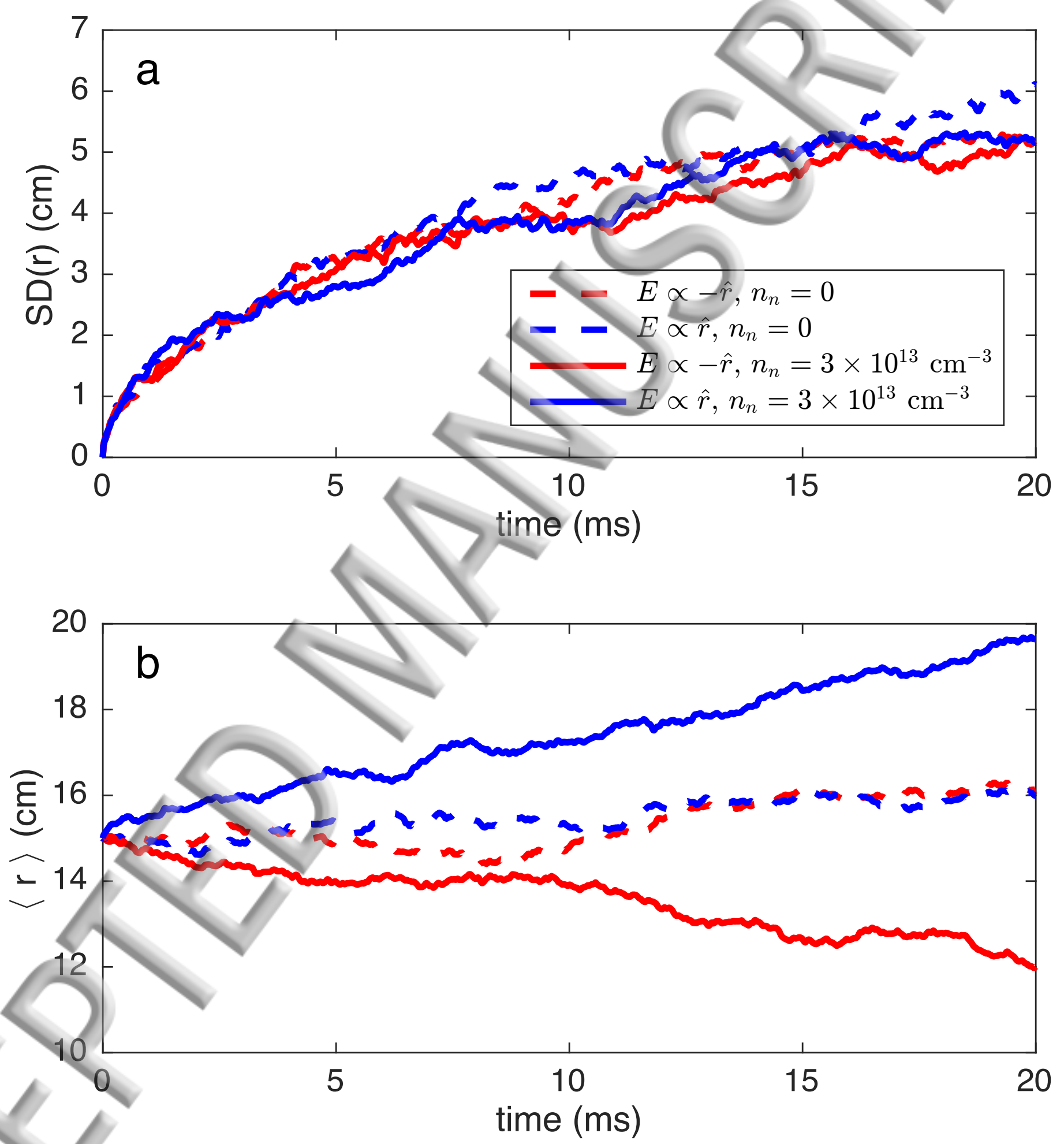

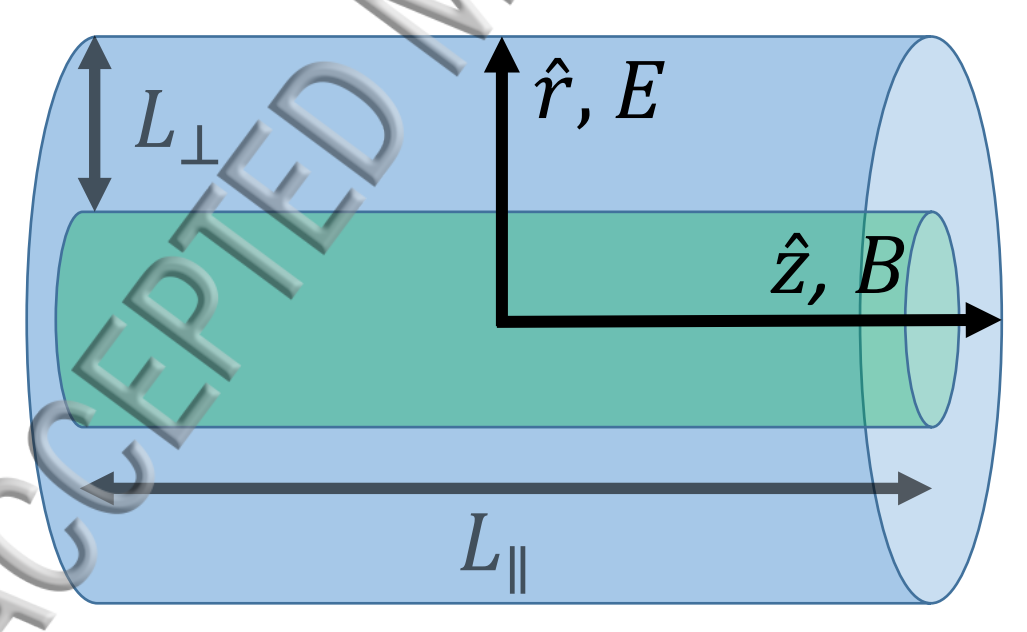

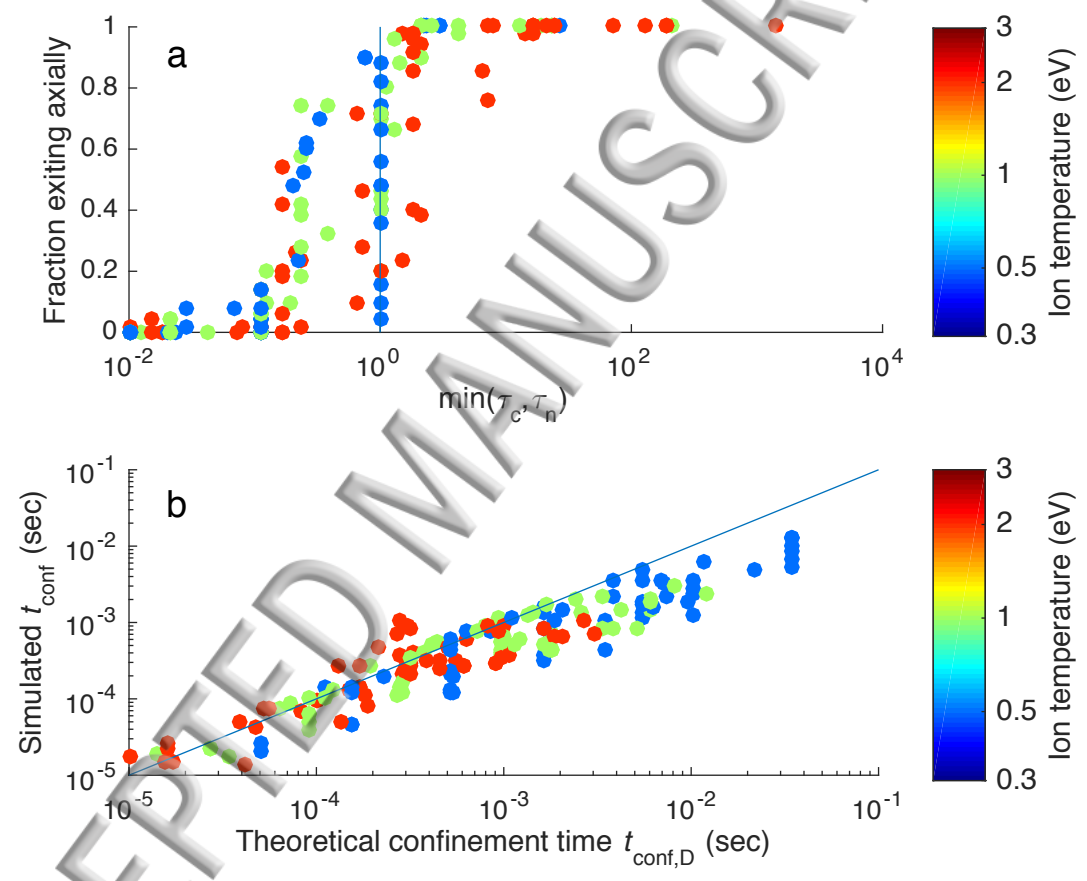

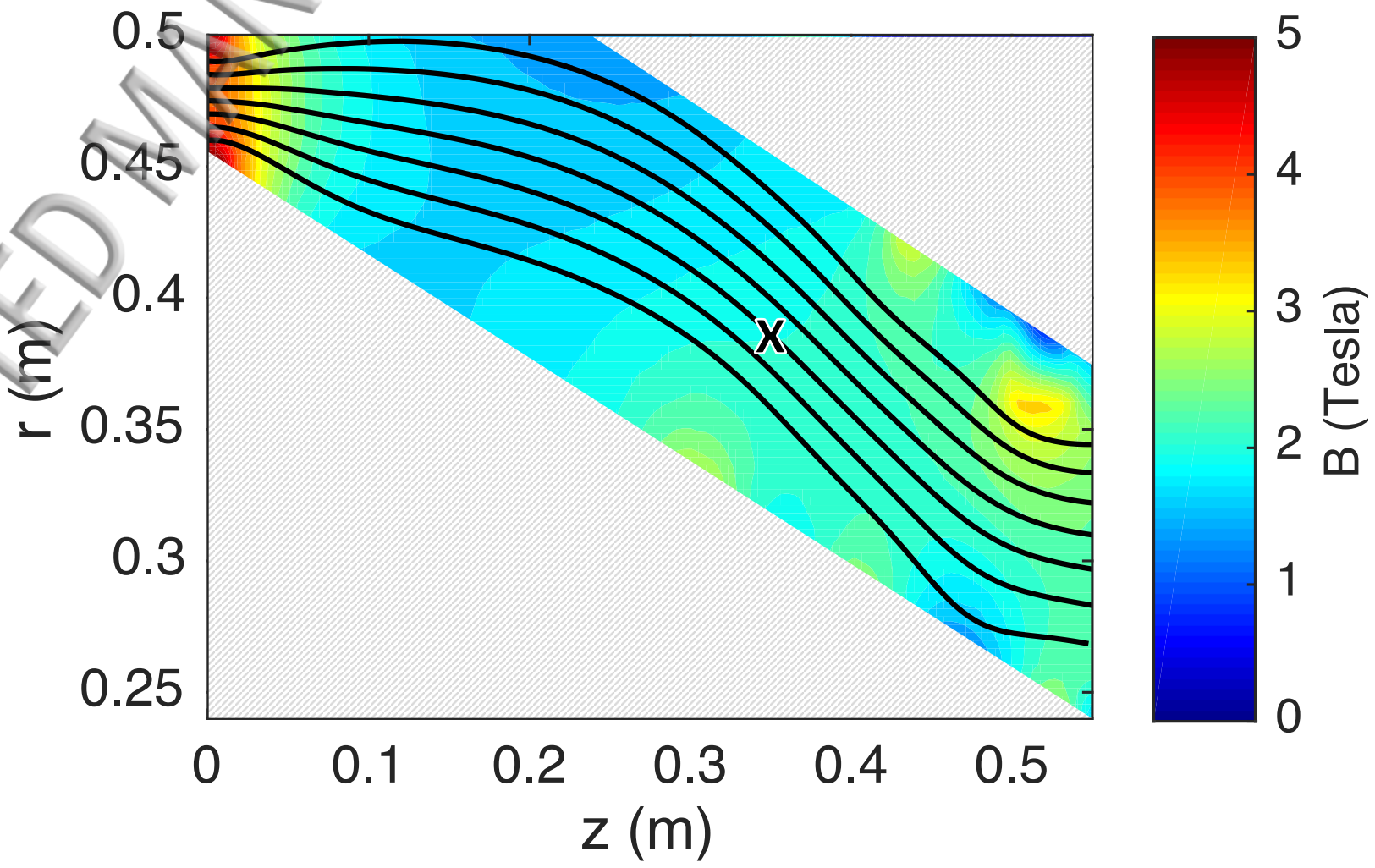
0.5
0.45
0.4
0.35
0.3
0.25
r (m)
0
0.1
0.2
0.3
0.4
0.5
z (m)
X
5
4
3
2
1
0
B (Tesla)

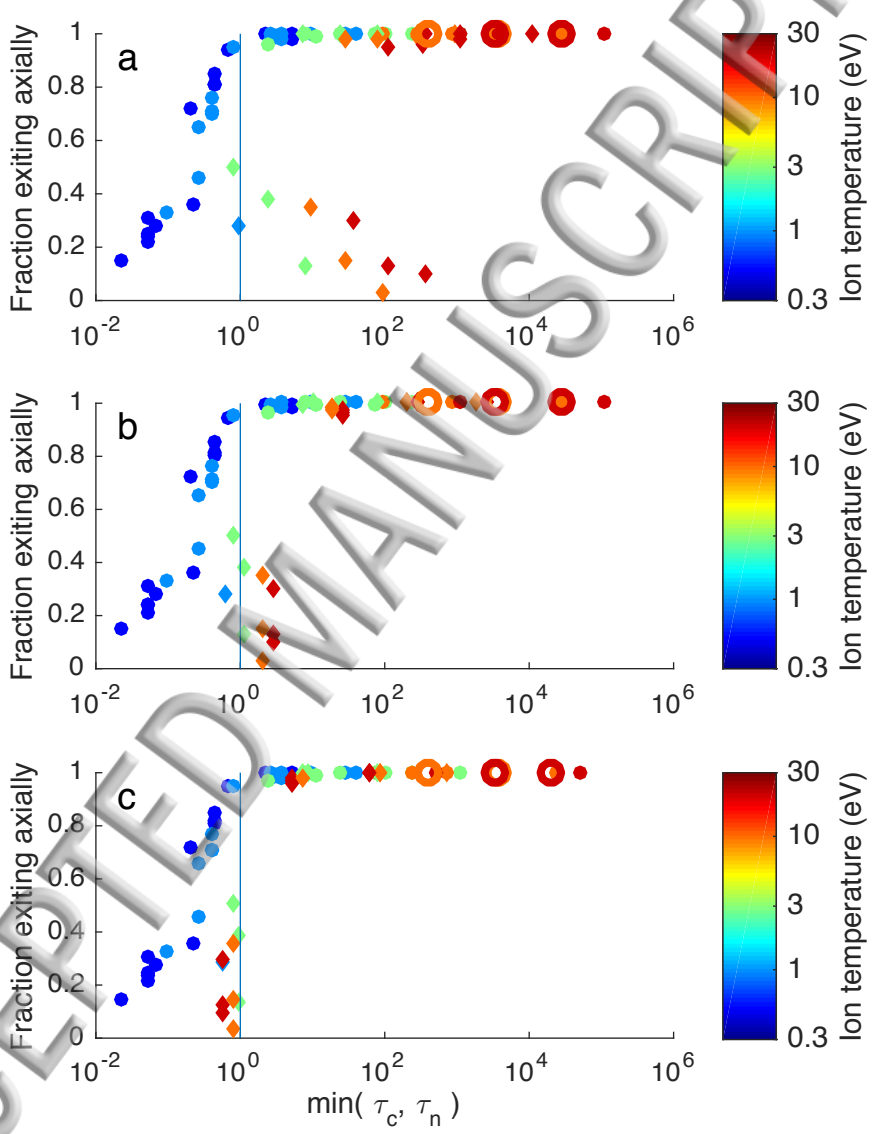

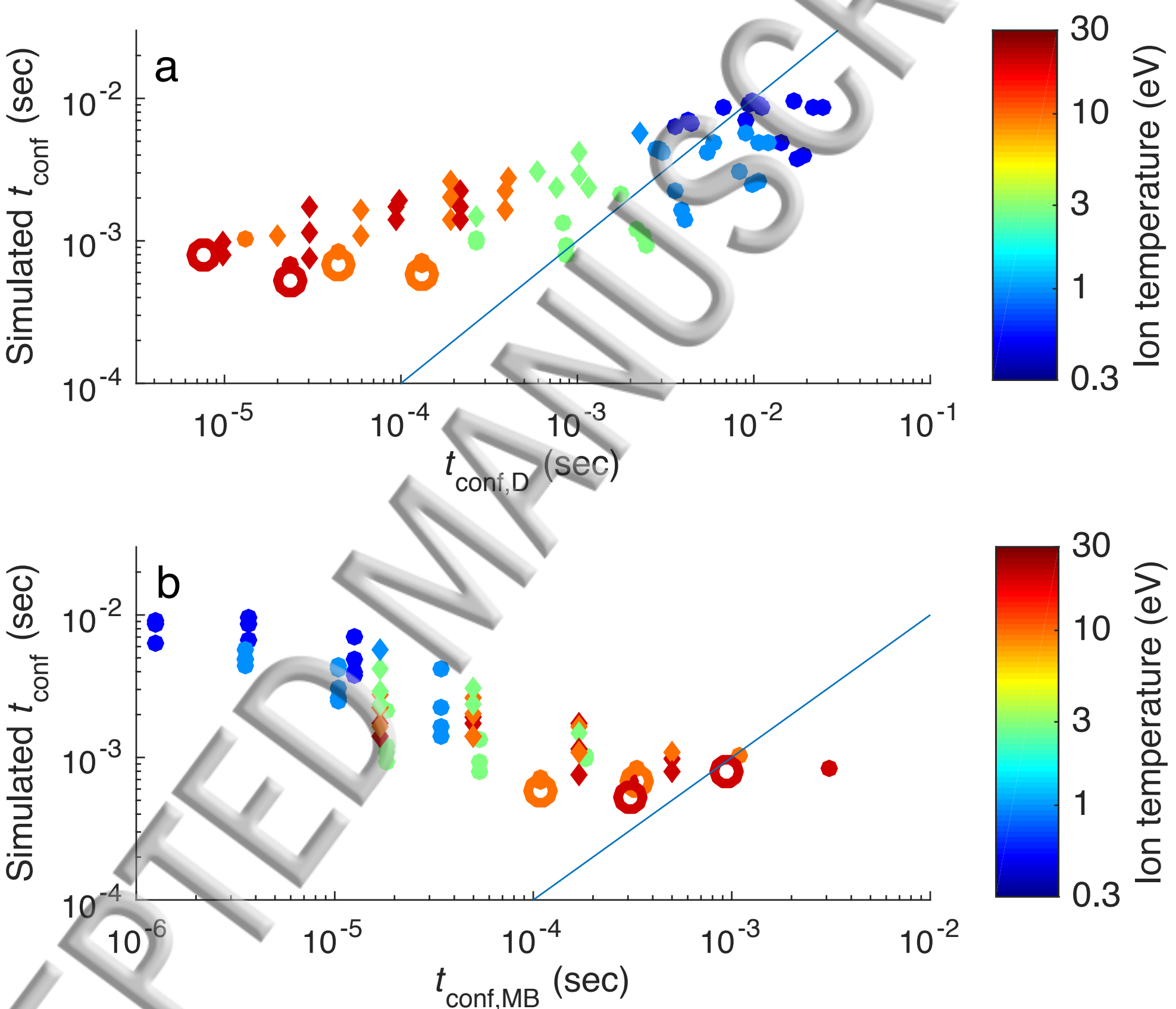

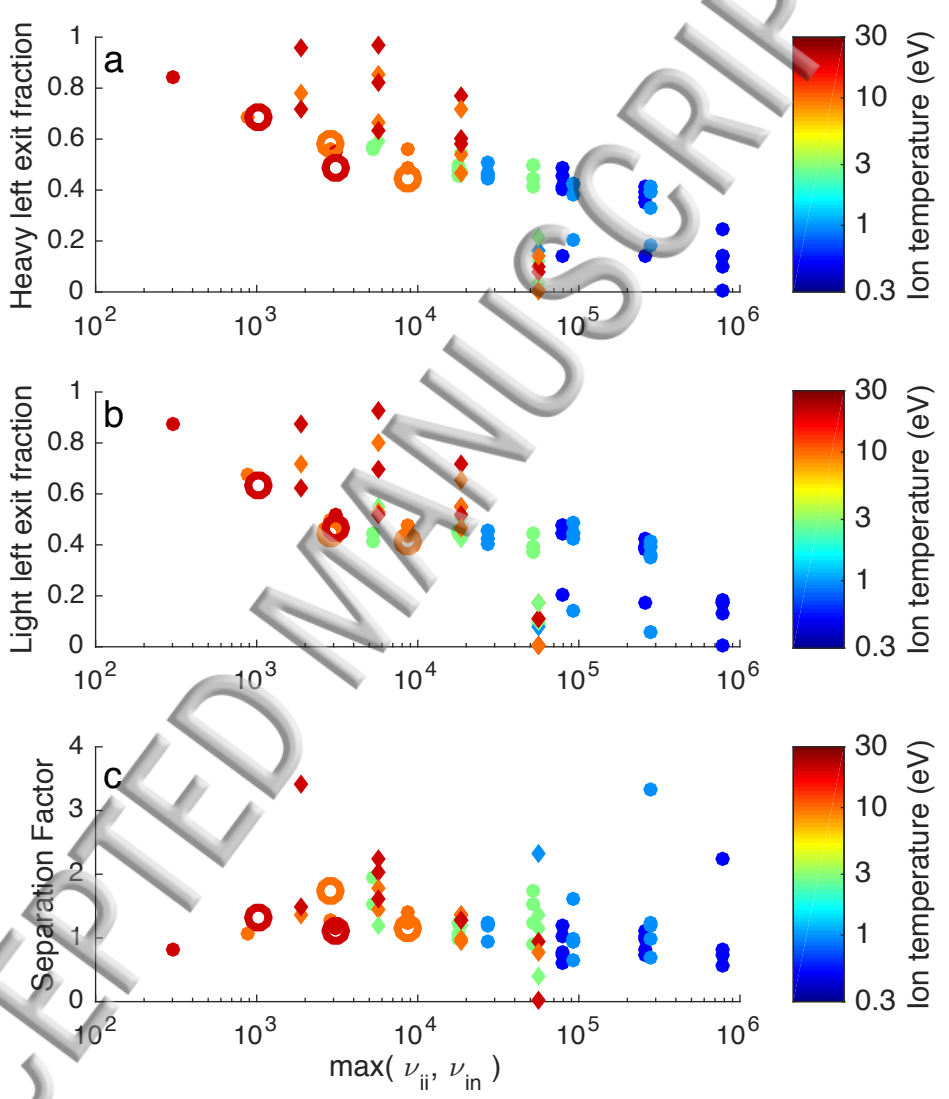

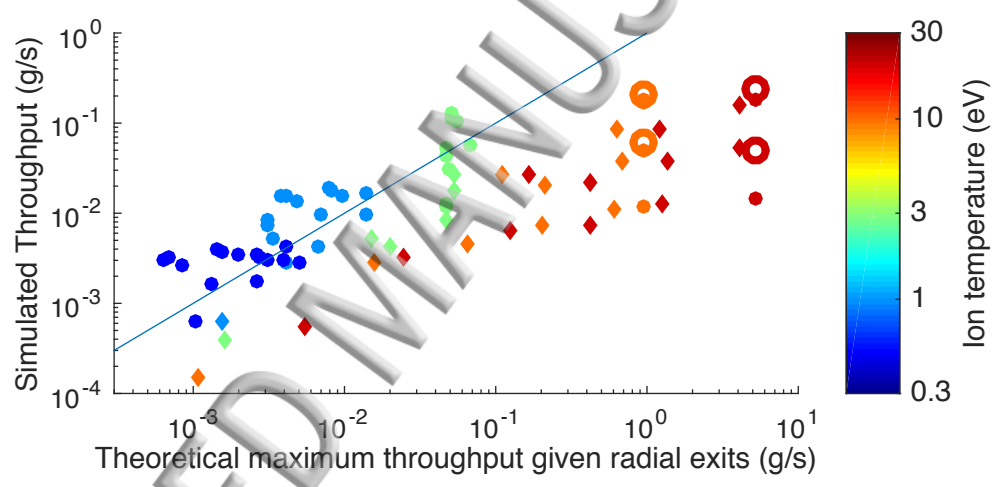
Simulated Throughput (g/s)
10^{0}
10^{-1}
10^{-2}
10^{-3}
10^{-4}
10^{-3}
10^{-2}
10^{-1}
10^{0}
10^{1}
Theoretical maximum throughput given radial exits (g/s)
Ion temperature (eV)
30
10
3
1
0.3